

# **Chapter 1**

## **Global Heterogeneity of the Lithosphere and Underlying Mantle: A Seismological Appraisal Based on Multimode Surface-Wave Dispersion Analysis, Shear-Velocity Tomography, and Tectonic Regionalization**

**A.J. Schaeffer and S. Lebedev**

**Abstract** Heterogeneity of the composition and physical state of the rocks within the Earth is reflected in variations in seismic wave speeds at depth. This seismic heterogeneity can be observed in a number of different ways, each yielding a complementary perspective on the Earth's bulk properties, structure, and dynamics. A surface-wave dispersion diagram, constructed from millions of fundamental-mode and higher mode dispersion measurements around the world, shows variability around global averages for all modes and all frequencies that are included in it, with the largest variations seen for the fundamental-mode phase and group velocities at short periods (less than 30 and 40 s, respectively) that sample the highly heterogeneous crust and uppermost mantle. Seismic tomography turns large sets of measurements into models of three-dimensional wave speed variations at depth. Global shear-wave speed models have been in agreement since 1990s regarding heterogeneity in the upper mantle at thousands-of-kilometres scales. The rapid recent increase in global data sampling facilitated an increase in the tomographic resolution, and a number of today's models show close agreement in the upper 200 km of the mantle at much shorter, hundreds-of-kilometres scale lengths. Greater disagreements between different models remain in the mantle transition zone. Our new model SL2013sv, constrained by an unprecedentedly large new data set of multimode waveform fits, demonstrates increased resolution compared

---

A.J. Schaeffer (✉) · S. Lebedev

Geophysics Section, School of Cosmic Physics, Dublin Institute for Advanced Studies,  
Dublin, Ireland  
e-mail: [aschaeff@cp.dias.ie](mailto:aschaeff@cp.dias.ie)

to other existing models for a variety of features; it captures regional-scale heterogeneity globally, within both the upper mantle and the crust. A global stack of shear-velocity profiles extracted from SL2013sv shows a monotonic decrease in the amplitude of wave speed variations with depth, mirrored by a decrease in RMS variations in SL2013sv and other current models, from largest in the top 150–200 km to much smaller below 250 km. Regionalization of SL2013sv by means of cluster analysis, with no *a priori* information, provides an accurate tectonic regionalization of the entire Earth. The three oceanic and three continental types that naturally come out of the clustering differ by the age of the deep lithosphere. The results give a new perspective on the “depth of tectonics”—the depths down to which shear speed profiles (and, by inference, geotherms) beneath oceanic and continental regions of different ages are different. Old oceanic plates are underlain by higher shear-wave speeds compared to young- and intermediate-age oceans down to 200 km depth. At 200–250 km, all type-average mantle profiles converge, except for the Archean craton profile that shows distinctly higher velocities down to 250–280 km depths.

**Keywords** Lithosphere dynamics • Mantle heterogeneity • Waveform inversion • Seismic tomography

## 1.1 Introduction

The speeds of seismic waves travelling through the Earth vary across a broad range of scales, from the crystals that make up rocks, the tectonic blocks that make up the continents, up to the scale of entire tectonic plates. This wave-speed heterogeneity is a consequence of heterogeneity in the composition and physical state of the rocks at depth. Mapping the variations of seismic wave speeds within the Earth—with seismic tomography or other methods—thus provides snapshots of the three-dimensional structure of the Earth’s interior, most of it inaccessible for direct sampling, and yields important clues on the dynamic processes within the planet.

One-dimensional (1D) reference seismic models (PREM: Dziewonski and Anderson 1981; AK135: Kennett et al. 1995) capture the key changes of seismic velocities with depth. These radial changes reflect the compositional stratification within the Earth, phase transformations in minerals to their higher pressure polymorphs with increasing depth, and the gradual increases of elastic moduli with pressure.

Seismic-velocity profiles beneath different points at the surface are different from the reference profiles and from one another. This lateral heterogeneity is manifested clearly in seismic observations. Seismic tomography uses these observations to constrain three-dimensional (3D) models of seismic-velocity variations at regional or global scales, offering insight into the basic mechanisms of plate tectonics and patterns of mantle convection.

Tomographic studies using surface and body waves in the late 1970s and early 1980s (Aki et al. 1977; Dziewónski et al. 1977; Kovach 1979; Woodhouse and Dziewónski 1984) demonstrated lateral variations in seismic velocities within the lithosphere and asthenosphere globally. Since about two decades ago, the long-wavelength (several thousands of kilometres) features of the Earth's lithospheric and asthenospheric mantle at depths down to ~300 km have been well established and resolved consistently by various global models (Becker and Boschi 2002). Short- and intermediate-wavelength heterogeneities (Kennett 1987; Wu and Flatte 1990; Nolet et al. 1994) have been more difficult to resolve uniformly at a global scale, although many of the prominent features of upper-mantle heterogeneity—including subducting slabs, spreading centres, or hot spots—have been imaged in numerous regional- and larger-scale studies.

At the global scale, variations in seismic velocity indicate and distinguish the main different types of lithosphere: oceanic versus continental. Within these two types, further variability is clearly seen, including the evolution of the oceanic plates from younger to older ocean basins (the latter with colder and thicker lithosphere, with higher seismic wave speeds within it) and differences between stable Precambrian cratons (high seismic velocities; particularly thick and cold lithosphere) and younger, Phanerozoic units. At regional scales, seismic imaging reveals deep expressions of active tectonic process, as well as preserved signatures of ancient ones. Beneath oceans, strong heterogeneity is observed in the vicinity of mid-ocean ridges (MOR), where new basaltic crust is generated through the extraction of melt from the mantle beneath the spreading centre and the newly created oceanic lithosphere cools rapidly as it moves further away from the ridge. At the opposite end of the plate cycle, strong heterogeneity can be observed beneath convergent plate boundaries, in subduction zones (e.g. around the Pacific Rim) or zones of continental collision (e.g. Tibet, Zagros).

The heterogeneity of seismic velocity in the Earth's upper mantle can be observed, first of all, directly in seismic measurements, for example, in variations of travel times of body waves or of phase and group velocities of surface waves as a function of the station and event locations. Secondly, heterogeneity can be examined in seismic tomography models constrained by the measurements. Bulk properties of these models, such as the RMS velocity anomaly as a function of depth, provide insight into the overall character of the heterogeneity. Visual and quantitative comparison of different tomographic models, computed by different groups using different methods, can provide further insight into the heterogeneous nature of the Earth's upper mantle. For example, the lithospheric mantle of several recent global tomographic models (Lebedev and van der Hilst 2008; Lekić and Romanowicz 2011a; Debayle and Ricard 2012; Schaeffer and Lebedev 2013) show agreement at significantly shorter length scales, compared to models of only a few years ago. Finally, regionalization analysis of seismic tomography models provides an objective subdivision of the Earth into regions with different properties within a given depth range. In the lithosphere–asthenosphere depth range, regionalization groups together geologic domains with similar deep structure, which—most often but with important exceptions—reflects similar tectonic evolution.

In this paper, we present views of the heterogeneity within the Earth’s crust and upper mantle from different perspectives, from measurements of phase and group velocities of multimode surface waves (particularly sensitive to the crust and upper mantle) to tomographic models and inferences from them. We utilize the very large phase- and group-velocity data set created in the course of the construction of our global tomographic model SL2013sv (Schaeffer Lebedev 2013), as well as the model itself. SL2013sv offers increased resolution globally, approaching that of regional-scale studies. The vertical component data set used to compute it consists of almost three quarters of a million waveform fits, from which more than half a million of the most mutually consistent seismograms were selected to constrain the model. Multimode phase velocities (the fundamental-mode and higher mode vertical component surface waves), measured as a by-product of the waveform fitting, span the broad period range from  $\sim$ 10 s to more than 400 s. Their distributions with period and their variability with source and station locations provide an empirical sampling of the bulk dispersion properties of the Earth’s upper mantle. We also explore the heterogeneity of the Earth’s upper mantle through examination of the salient features in the model SL2013sv, compare this view of the upper mantle with that from other recent tomographic models, and discuss inferences from global tomography regarding the structure and dynamics of the crust and upper mantle.

## 1.2 Heterogeneity in Measurements of Phase and Group Velocities of Multimode Surface Waves

Surface waves are highly sensitive to the structure of the crust and upper mantle. Due to the frequency dependence of their depth sensitivity—and, consequently, frequency dependence of their propagation speed (dispersion)—surface waves have two different measurable velocities: phase velocity and group velocity. Phase velocity ( $C(\omega)$ ) is the speed at which the phase at a particular frequency travels, whereas the group velocity ( $U(\omega)$ ) is the speed at which the energy of the wave packet propagates. With decreasing frequency (increasing period), surface waves sample greater depths within the subsurface: short periods (high frequencies) are sensitive to crustal structure, whereas longer periods are sensitive to depths near the base of the upper mantle (see Fig. 1.1). The fundamental mode of Rayleigh or Love surface waves is typically the most energetic arrival on a vertical- or horizontal-component seismogram, respectively. Higher surface-wave modes interfere constructively to produce the arrivals of body waves ( $P$  and  $S$  waves) and their multiple surface reflections (e.g. SS, SSS, SSSS)—a manifestation of the ray-mode duality (Dahlen and Tromp 1998). Each of the modes has a different frequency-dependent depth sensitivity; together, they provide rich information regarding the structure within the Earth.

Variations in surface-wave dispersion measured along different source-station paths provide a direct indication of structural heterogeneity and lateral variations

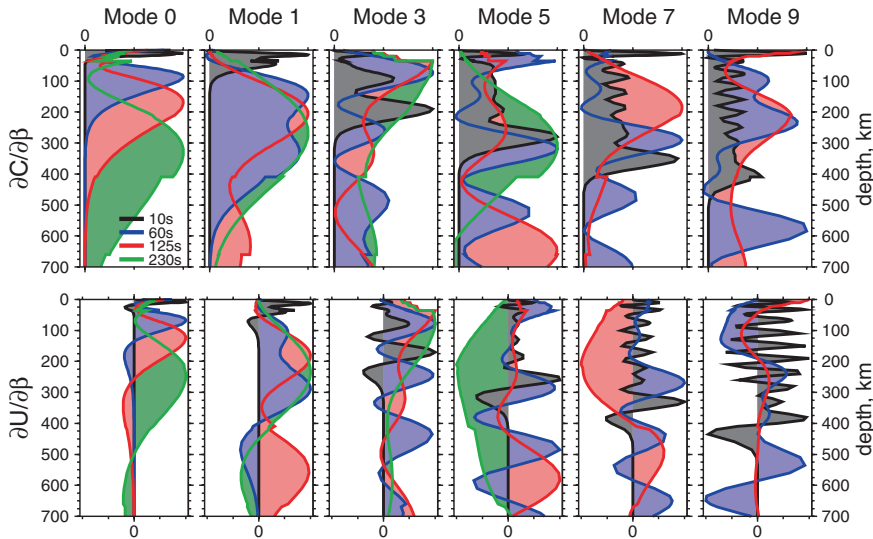


**Fig. 1.1** Depth sensitivity kernels of the Rayleigh-wave phase and group velocities, computed for AK135. The derivatives are with respect to shear velocity,  $\partial C(\omega)/\partial \beta$  and  $\partial U(\omega)/\partial \beta$ , at four periods 10 s (dark grey), 60 s (blue), 125 s (red), and 230 s (green), for the fundamental mode and the first, third, fifth, seventh, and ninth overtones. The amplitude of each kernel is scaled independently to its maximum within the depth interval. Note that for modes seven and nine at 230 s, there is no sensitivity within this depth range

in the elastic properties of the crust and mantle. As the depth sensitivity of the modes is known, the measurements at different periods can be viewed as expressions of heterogeneity at different depths.

In order to examine bulk distributions of phase and group velocities globally, we use the data set generated using the Automated Multimode Inversion (AMI; Lebedev et al. 2005) of surface and  $S$  waveforms in the course of construction of the global tomographic model of Schaeffer and Lebedev (2013) (Sect. 1.3).

As a by-product of successfully fitting a seismogram, AMI measures phase velocities for the modes which contribute significantly to the waveform fit within the time–frequency windows that were selected. The group velocity ( $U(\omega)$ ) can then be computed from the phase velocity ( $C(\omega)$ ) using:

$$U(\omega) = \frac{C(\omega)}{1 - \left( \frac{\omega}{C(\omega)} \right) \left( \frac{dC}{d\omega} \right)}, \quad (1.1)$$

where  $\omega = 2\pi/T$  is the angular frequency and  $T$  is the period.

The data set used to constrain the model SL2013sv consists of 712,504 waveform fits computed for vertical component seismograms recorded up to March 2010. Here, we augmented it with an additional 239,462 fits computed for seismograms recorded until June 2012. In total, the data set is formed by more than

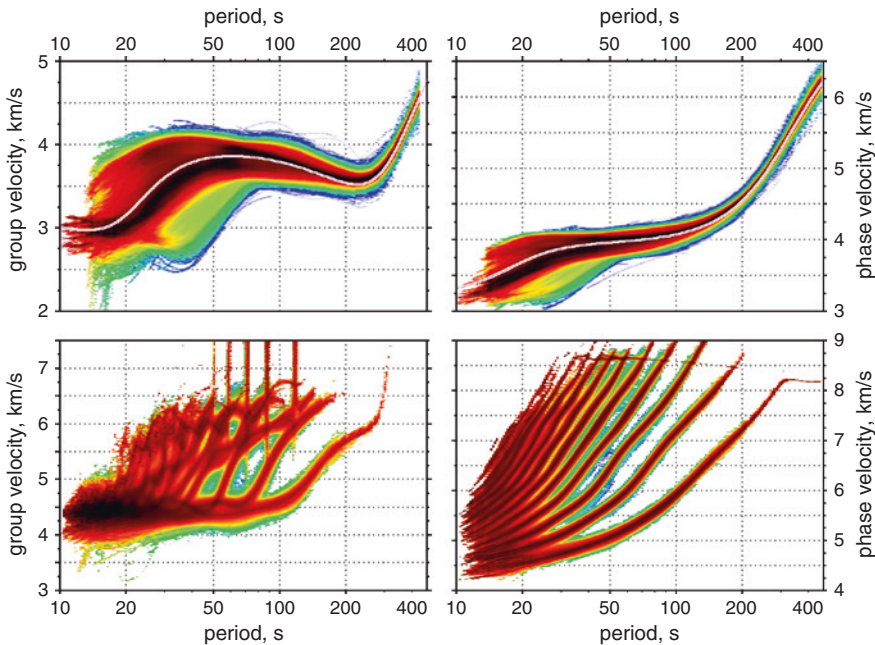


**Fig. 1.2** Empirical dispersion diagrams of Rayleigh waves on the Earth. Fundamental-mode (top row) and higher mode (bottom row) Rayleigh-wave group-velocity (left column) and phase-velocity (right column) curves were measured by AMI after (successful) waveform fitting. Increased sampling density of phase or group velocity is indicated by warming colours from blues through reds to black; the sampling density is normalized for each period. Over-plotted in the fundamental-mode panel are the dispersion curves computed for AK135

951,000 vertical component waveform fits (951,000 seismograms). It yields more than 951 thousand fundamental-mode and ~480 thousand higher mode, Rayleigh-wave, phase-velocity—and therefore group-velocity—curves, across a broad period range of 10–450 s. The criteria required to generate a waveform fit result in a fundamental-mode dispersion curve for every successfully fit seismogram; the total frequency band of each dispersion curve varies on a case-by-case basis.

Although these dispersion curves are not used in the generation of the tomographic model, they can be used in other imaging studies, such as array-based teleseismic interferometry utilizing the fundamental mode (e.g. Deschamps et al. 2008; Darbyshire and Lebedev 2009; Zhang et al. 2009; Endrún et al. 2011; Adam and Lebedev 2012, to name a few) and, potentially, higher modes.

In Fig. 1.2, we plot the fundamental-mode and higher mode phase- and group-velocity curves, as in Nolet (2008), from our data set of ~512 thousand multimode Rayleigh-waveform fits used to constrain SL2013sv. The individual dispersion curves were binned, such that the blue colours represent the lowest density sampling (white means not sampled), whereas warmer colours indicate increasing density; black represents the highest density velocity at each period.

The group-velocity curves were computed from the phase velocity ones, using Eq. 1.1. In the fundamental-mode windows, the superimposed lines indicate the dispersion curves computed for AK135.

The inclusion of higher modes is critical for maintaining resolving power at the base of the upper mantle and in the transition zone. This sensitivity is given by  $S$  and multiple  $S$  waves that bottom throughout this depth range and represents a superposition of multiple higher modes. Our complete data set contains many tens of thousands to a hundred thousand dispersion curves for each of higher modes one through eight, thousands for modes up to ten, and relatively minor contributions from those modes beyond (<0.05 % from modes 11–20). The impact of the inclusion of these higher modes (i.e.  $S$  and multiple  $S$  waves) on the tomographic resolution in the deep upper mantle and transition zone is illustrated in Figs. 4 and 5 of Lebedev et al. (2005), who performed the waveform fitting first for the fundamental mode only, second for the fundamental mode and  $S$  waves, and finally for the fundamental mode and  $S$  and multiple  $S$  waves. As more  $S$  wave information is added, the eigenvalues drop off less rapidly, indicating greater structure in the resulting path-average model, as can also be seen in the shear-velocity models in their Fig. 4.

The global variability of the fundamental-mode and higher mode dispersion curves offers a perspective on the bulk heterogeneity within the Earth's upper mantle. At a given period, the total spread in velocity indicates an empirical range of Earth properties, whereas the relative distribution in colour across the velocity band indicates which velocities are most common—subject to the sampling filters imposed by the distribution of the stations and events and by the averaging over the Frénel zones between the sources and stations.

For the fundamental-mode group velocities (top left, Fig. 1.2), the strongest variability is at periods less than 45 s, with a transitional band between 45 and 80 s, and reduced variability at periods beyond 80–100 s. The total spread in velocity decreases by a factor of 2 at long periods compared to short periods. This results from the increased sensitivity of the long periods to greater depths, at which heterogeneity is weaker than at shallow, crustal depths. A similar pattern can be observed for the fundamental-mode phase velocity (top right panel), however, with the transition shifted to slightly shorter periods due to the differing depth sensitivities of group and phase velocities (e.g. Lebedev et al. 2013).

At the shorter periods sampling the crust and uppermost mantle, the relatively strong heterogeneity is readily apparent. In continental regions, this shorter period band is most sensitive to the crustal structure; we observe that the densest sampled velocities at these periods less than 50–60 s (35–45 s for phase velocity) are slower than AK135. In regions where the Moho is at greater depths (beneath orogenic belts, for example), the low velocities extend to longer periods, which is seen as the yellow-green colours well below AK135 at 30–75 s and 30–50 s periods for group and phase velocities, respectively. In oceanic regions, the Moho is much shallower and the fundamental mode at 15–30 s period samples the uppermost mantle rather than the crust; it is thus faster than in AK135.

At periods shorter than 50 s, the dispersion-curve representation of heterogeneity is affected by a sampling bias, with the most sampled velocities similar to or slower than AK135. This is not what would be expected when looking at the relative surface areas of oceans versus continents. In fact, one would expect greater sampling of high velocities (relative to AK135) in this period band, representative of the fast uppermost mantle beneath oceans, as there is a larger proportion of oceans than continents. However, this is opposite to what we observe, with the densest sampling at velocities slower than AK135. This discrepancy is explained simply by the distribution of stations and events, dominated by paths shorter than 4000–5000 km, which results in preferential sampling of continental and backarc regions.

### 1.3 Global Heterogeneity of the Upper Mantle and the Crust from Multimode Surface-Wave Tomography

We now explore the heterogeneity of the Earth's upper mantle using the tomographic model SL2013sv (Schaeffer and Lebedev 2013). This model is parameterized on a global triangular grid (Wang and Dahlen 1995) with an average spacing of ~280 km (minimum 250 km, maximum 290 km) and is constrained by the ~520 thousand vertical component seismograms selected from more than 710 thousand successful waveform fits, as the most mutually consistent data.

The model was computed using the Automated Multimode Inversion (AMI; Lebedev et al. 2005) that performs automated, accurate processing of large numbers of vertical- and horizontal-component broadband seismograms. The result of each successful waveform inversion is a set of linear equations with uncorrelated uncertainties (Nolet 1990, 2008) that describe 1D perturbations in elastic structure within a finite-width sensitivity volume between the source and receiver relative to a three-dimensional (3D) reference model (Lebedev and van der Hilst 2008; Schaeffer and Lebedev 2013). Synthetic seismograms are computed using the JWKB approximation by summing over modes ( $m$ ), with the phase velocity of mode  $m$  given by  $C_m^0(\omega) + \overline{\delta C_m(\omega)}$ , where  $C_m^0(\omega)$  is the average initial phase velocity within the sensitivity volume and  $\overline{\delta C_m(\omega)}$  is the average phase velocity perturbations. These are expressed as a function of the sensitivity-volume average perturbations in  $P$  and  $S$  velocity ( $\overline{\delta\alpha(r)}$  and  $\overline{\delta\beta(r)}$ , respectively):

$$\overline{\delta C_m(\omega)} = \int_0^R \frac{\partial C_m^0(\omega)}{\partial \beta(r)} \overline{\delta\beta(r)} dr + \int_0^R \frac{\partial C_m^0(\omega)}{\partial \alpha(r)} \overline{\delta\alpha(r)} dr, \quad (1.2)$$

where  $R$  is the radius of the earth and  $\partial C_m^0(\omega)/[\partial\beta(r), \partial\alpha(r)]$  are the Fréchet derivatives. The sensitivity-volume-average perturbations in seismic velocity ( $\overline{\delta\beta(r)}, \overline{\delta\alpha(r)}$ ) are thus related to the synthetic waveform  $s(\omega)$  through the average phase velocity

perturbation  $\overline{\delta C_m(\omega)}$ . The  $\overline{\delta\beta(r)}$  (and equivalently the  $\overline{\delta\alpha(r)}$ ) are parameterized with  $M$  model parameters  $\gamma_i$  on a set of 1D triangular basis functions  $h_i(r)$  which span from the crust to the lower mantle (7–1600 km),  $\overline{\delta\beta(r)} = \gamma_i h_i(r)$ . AMI then produces a set of linear equations with uncorrelated uncertainties:

$$\overline{\delta\beta(r)} = \eta_j g_j(r), \quad (1.3)$$

where each  $g_j(r)$  is a linear combination of the original basis functions (see Nolet 1990, 2008; Lebedev et al. 2005; Lebedev and van der Hilst 2008; Schaeffer and Lebedev 2013, for further details).

A large system is constructed using the independent linear equations generated by AMI (the  $\eta_j$  from Eq. 1.3 for each path), with the waveform structural information mapped into the model parameters using the same approximate sensitivity kernels as used in the waveform inversion by AMI, and is then solved for 3D perturbations in isotropic  $S$  and  $P$  velocity with respect to the 3D reference model and  $2\Psi$  azimuthal anisotropy of  $S$  velocity (see Schaeffer and Lebedev 2013 for details on the data set and model construction).

In Figs. 1.3 and 1.4, we plot 12 horizontal slices through the model, at depths of 36, 56, 80, 110, 150, and 200 km (Fig. 1.3), and 260, 330, 410, 485, 585, and 660 km (Fig. 1.4). The perturbations (as indicated beneath each slice) are with respect to a 3D reference model. At depths greater than the Moho (Moho depth is position dependent), perturbations are in per cent, relative to the global 1D mantle reference model (a modified AK135, Lebedev and van der Hilst 2008; Schaeffer and Lebedev 2013). At depths shallower than the Moho (some regions in the slices at 36 and 56 km depth), model perturbations are indicated in  $\text{m s}^{-1}$  and are relative to the 3D crustal model (modified CRUST2); in these regions, only the perturbation in  $\text{m s}^{-1}$  is correct. Although this makes interpretation of the strength of velocity perturbations in crustal regions more complex, the relative variations are still readily interpreted in terms of heterogeneity and structure.

This new model provides improvements, compared to other existing models, in the resolution of fine-scale regional features through much of the upper mantle and transition zone. At the longer wavelengths, lithospheric-depth structures broadly agree with observations from numerous past models utilizing varying methodologies, parameterizations, and data sets (both type and size) (e.g. Debayle et al. 2005; Zhou et al. 2006; Houser et al. 2008; Kustowski et al. 2008; Lebedev and van der Hilst 2008; Nettles and Dziewónski 2008; Panning et al. 2010; Ferreira et al. 2010; Lekić and Romanowicz 2011a; Ritsema et al. 2011; Debayle and Ricard 2012). At greater depths in the sub-lithospheric mantle and transition zone however, larger variations between models are evident even at the longer wavelengths (thousands of kilometres, e.g. Ritsema et al. 2011).

In the following sections, we examine some of the prominent features in SL2013sv that exhibit deep expressions of tectonic structures and processes, including spreading ridges and subduction zones. The strongest shear-speed anomalies are observed beneath mid-ocean ridges (MORs) and rift systems (negative),

backarcs and active orogens (negative), stable continental cratons (positive), and within subducted lithosphere (positive).

### 1.3.1 Spreading Ridges

As observed in the shallow mantle in the horizontal sections (Fig. 1.3), spreading ridges globally are resolved as narrow anomalies directly beneath the ridge axis.

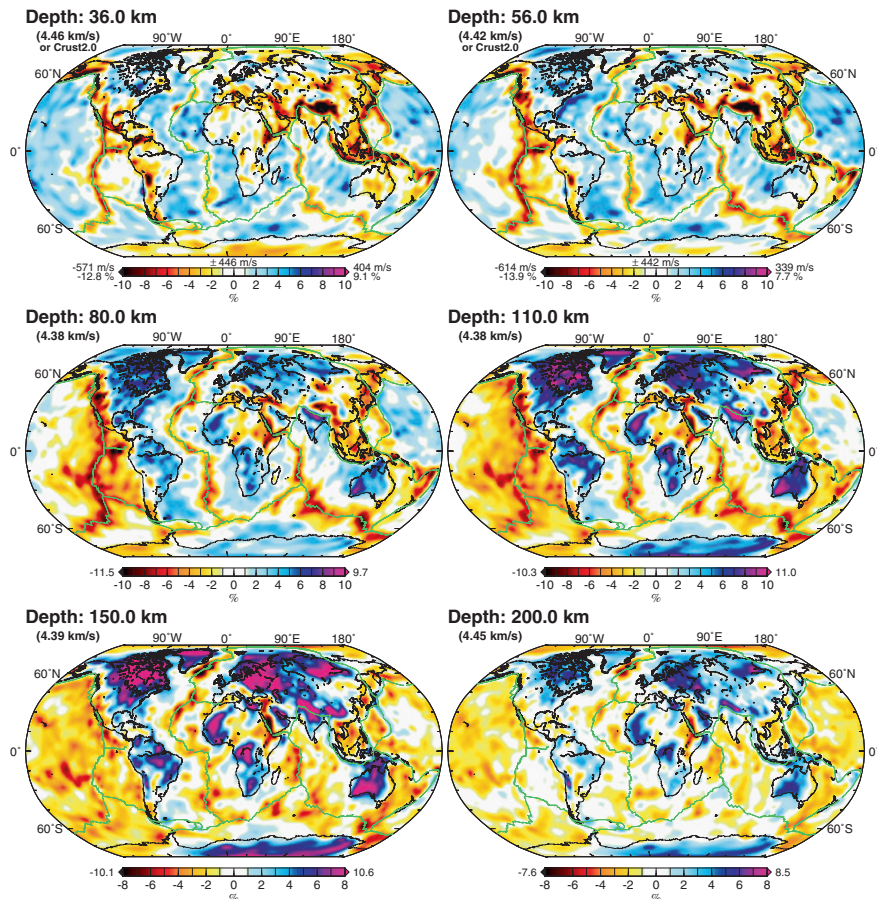


**Fig. 1.3** Horizontal slices through SL2013sv at six depths in the crust and uppermost mantle: 36, 56, 80, 110, 150, and 200 km. The reference velocity is indicated in brackets beneath each depth, and perturbations are plotted with respect to this value, for locations beneath the Moho. The minimum and maximum perturbations are indicated at the edges of the saturated-scale bar. For the depths 36 and 56 km, some locations are still in the crust, and therefore, perturbations are instead in  $\text{m s}^{-1}$  with respect to our 3D crustal reference model (modified CRUST2), as indicated above the colour scales. Plate boundaries are indicated by green lines

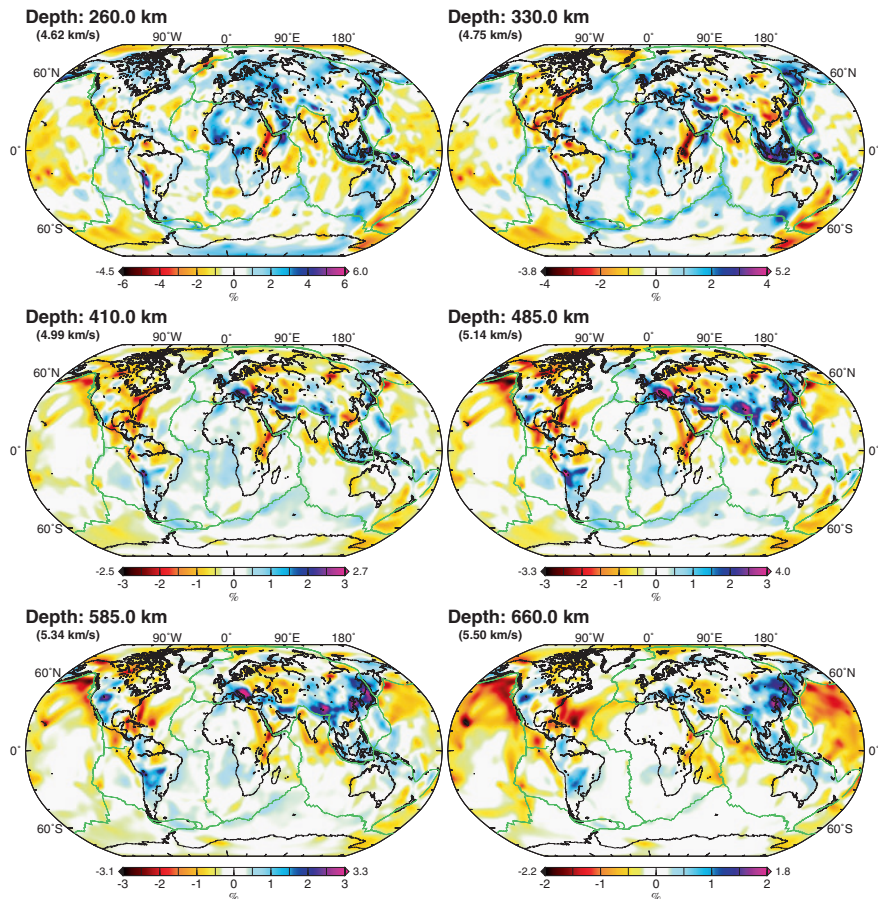


**Fig. 1.4** Horizontal slices in the sub-lithospheric mantle and transition zone: 260, 330, 410, 485, 585, and 660 km. Reference velocity and perturbations are as in Fig. 1.3

With increasing depth, from 36 to 80 km, the anomalies increase in amplitude and also broaden in extent from the spreading centre. The very strong negative anomalies are indicative of the presence of partial melt. Continuing to greater depths, from 110 to 150 km, the anomalies broaden and also decrease in amplitude. By 150 km depth, the central low-velocity zone no longer stands out from the surrounding oceanic asthenosphere. At depths greater than 120–130 km, partial melting may still take place, but with a lower degree, no longer visible in the vertically polarized shear velocity. This is in agreement with some past studies (e.g. Zhang and Tanimoto 1992; Forsyth et al. 1998), but does not confirm the inferences in other studies (e.g. Su et al. 1992), suggesting that MOR processes extend into much deeper upper mantle.

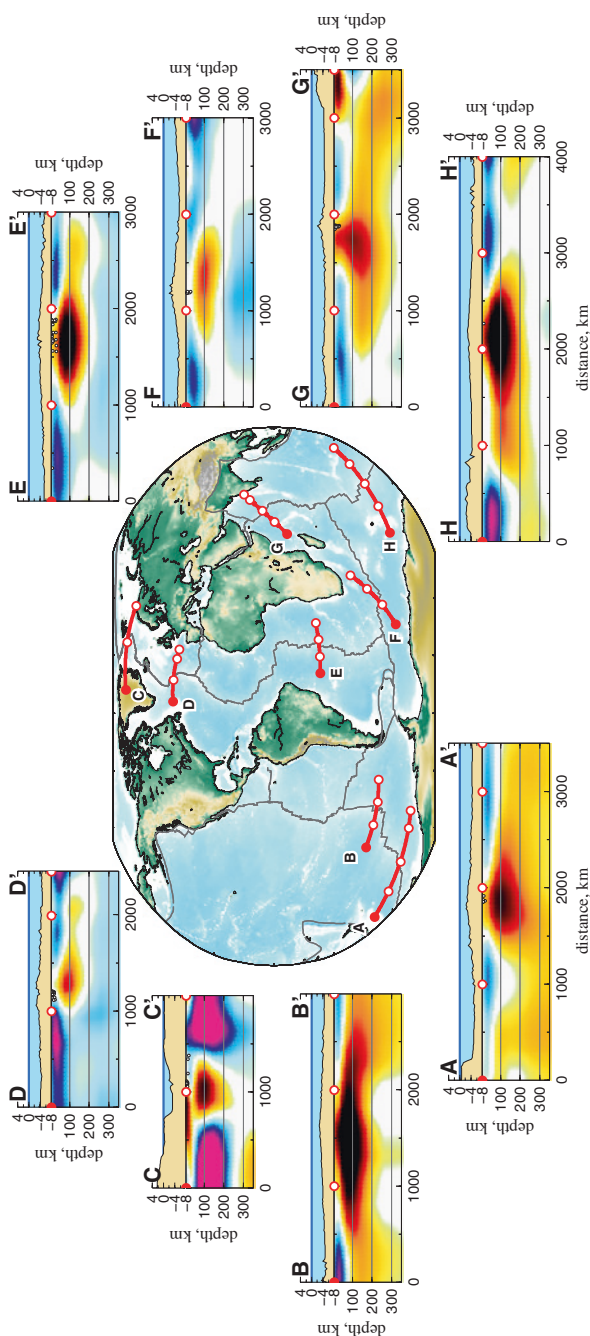


**Fig. 1.5** Vertical cross sections through “normal” spreading ridge segments. Above each slice through the model SL2013sv, topography is plotted with tick marks denoting elevations (or bathymetry) spaced at 4 km. Horizontal distance between red circles (both on map and each cross section) is 1000 km; the closed red circle marks one end of each section to indicate orientation. The (saturated) colour scale is the same in each cross section, with  $\pm 220 \text{ m s}^{-1}$  limits

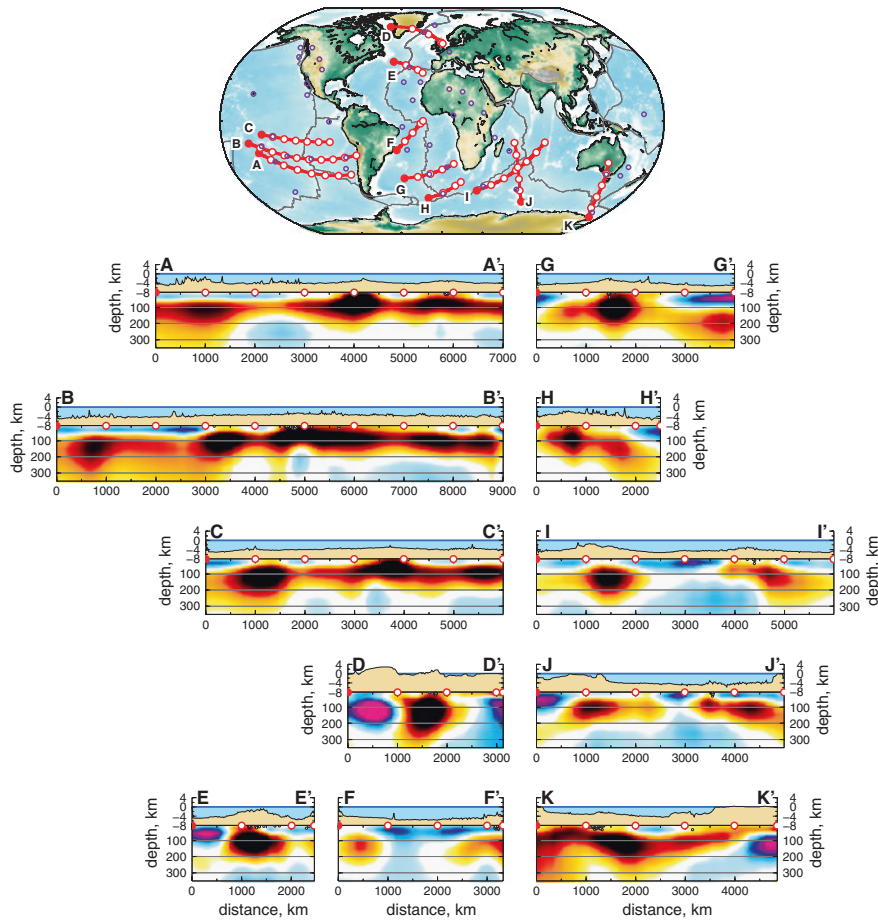


**Fig. 1.6** Vertical cross sections through spreading ridges with nearby hot spots. Above each slice through the model SL2013sv, topography is plotted with tick marks denoting elevations (or bathymetry) spaced at 4 km. Horizontal distance between *red circles* (both on map and each cross section) is 1000 km; the *closed red circle* marks one end of each section to indicate orientation. The (saturated) colour scale is the same in each cross section, with  $\pm 220 \text{ m s}^{-1}$  limits. Hot spots from the catalog of Steinberger (2000) are indicated by *purple circles* on the map

In Figs. 1.5 and 1.6, we plot vertical cross sections through spreading ridges around the globe. Each section spans from 7 to 350 km depth, with grid lines every 100 km. Topography/bathymetry is indicated above each section (extracted from ETOPO2), with tick marks every 4 km. Open red circles on both the map and each cross section are every 1000 km, and the closed red circle marks matching ends of the profiles to clarify the orientation. Seismicity within 40 km perpendicularly of the cross section is extracted from the EHB catalog (Engdahl et al. 1998) and plotted with white circles. Figure 1.5 shows “normal” cross sections, which demonstrate the expected triangular region of decompression melting beneath the

ridge axis. The cross sections in Fig. 1.6 highlight sections of ridges with non-triangular melting regions, as well as interactions with nearby hot spots.

In comparing the “normal” cross sections and indeed many of the asymmetric interacting cross sections, it is clear that the strongest spreading anomalies are confined to depths,  $\sim$ 150 km or less, and that the central anomaly clearly widens as a function of depth. Note that the saturations here are relatively higher than those in the horizontal cross sections and are in  $\text{m s}^{-1}$  rather than percentage. Beneath most of the ridges, sharp lateral boundaries between the ridge anomaly and the surrounding asthenospheric mantle delimit the central anomaly associated with high-degree partial melting.

Beneath the rapidly spreading EPR (Figs. 1.5A, B and 1.6A, B, and C), the velocity anomalies are the strongest and spread the widest, compared to other ridges around the globe. For those sections interacting with the nearby hot spots, several connected low-velocity anomalies are present. In profile 1.5B crossing the southern EPR, a single anomaly is present, with a width of approximately 2000 km, significantly wider than other “normal” spreading ridges.

### 1.3.2 Subduction Zones

Subducting lithospheric slabs clearly stand out in the horizontal sections, beginning at depths of 110–150 km (Fig. 1.3), beneath the Aleutians, Kuriles, Japan, Izu-Bonin, Mariana, Sumatra, Tonga-Kermadec-Hikurangi, and portions of the Andean. Additionally, smaller anomalies can be observed associated with subduction at the Cascadia, Lesser Antilles, and Scotia arcs. At greater depths and into the transition zone, a band of high velocities is observed extending almost continuously from Tibet through the Pamirs and Hindu Kush to Anatolia, and westwards to Central Europe. This material likely represents fragments of ocean basins, continental lithosphere, and continental margins, subducted in the final stages of the closure of the Tethys Ocean (Hafkenscheid et al. 2006; Schaeffer and Lebedev 2013).

In Fig. 1.7, we plot nine vertical cross sections through different subduction zones around the globe, including (A) Tonga and New Hebrides, (B) Sumatra-Java, (C) Ryuku and the Marianas, (D) Ryuku and Izu-Bonin, (E) Japan, (F) the Kuriles, (G) the Aleutians, (H) Central America and the Lesser Antilles, and (I) the Chilean segment of the Andean subduction zone.

In each cross section, a high-velocity anomaly can be seen dipping well into the upper mantle, corresponding with the overplotted seismicity (white circles). In addition to the high velocities associated with the subduction of fast oceanic lithosphere, low velocities are clearly observed in the backarc regions, reflecting the high water content in the mantle there. The strength and depth distribution of these anomalies varies between different subduction zones.

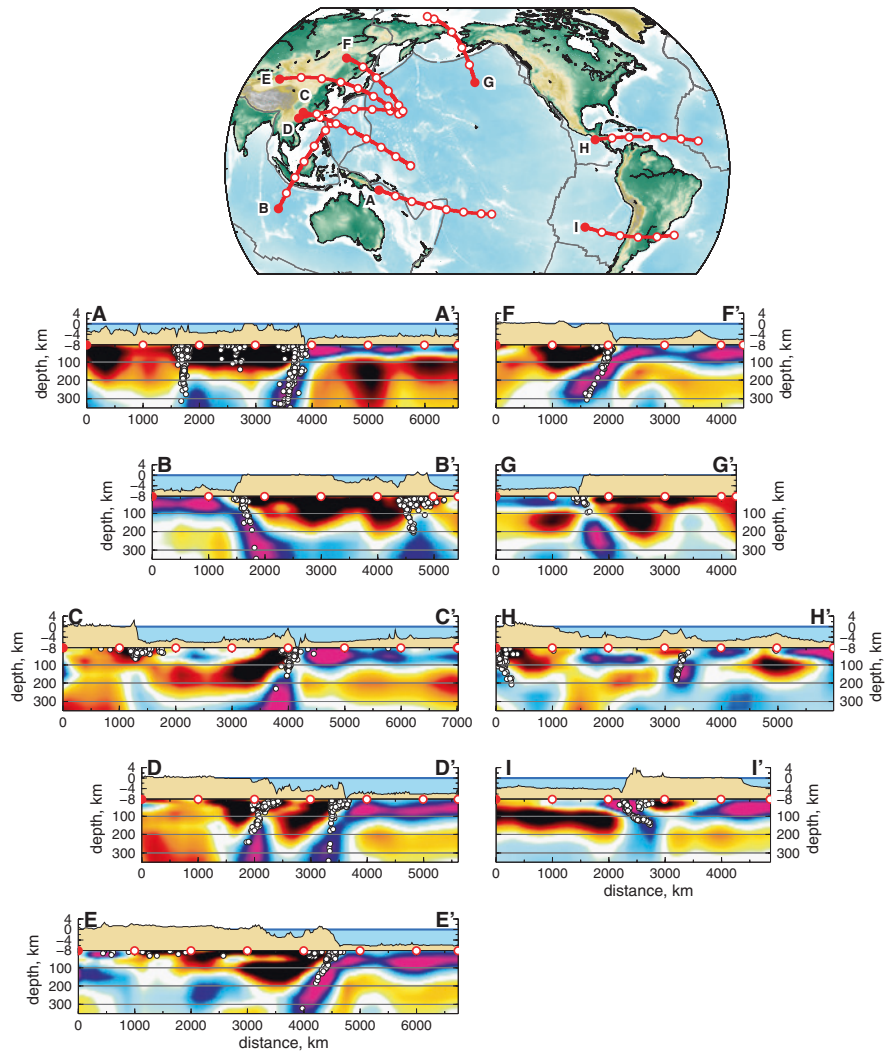


**Fig. 1.7** Vertical slices across subduction zones. Plotting set-up and conventions are as in Figs. 1.5 and 1.6

## 1.4 Tectonic Regionalization of the Upper Mantle

Over the last several decades, the number of available global tomography models has increased steadily; however, there has not been a comparable proliferation in tools to compare them (Lekić and Romanowicz 2011b). A common methodology was to compare harmonic spectra and examine at their correlation. The spectrum of model A is computed as follows:

$$S_A^2(\ell) = \sum_{m=-\ell}^{\ell} A_\ell^m A_\ell^{m*}, \quad (1.4)$$

where  $A_\ell^m$  are the spherical harmonic coefficients for degree  $\ell$  and azimuthal order  $m$ , and  $*$  denotes complex conjugation. Computing the spectral power at a range of depths and angular orders permits the construction of a 2D image depicting where the energy lies. This can then be extended to a harmonic correlation between two different models using

$$C_A^B(\ell) = \frac{\sum_{m=-\ell}^{\ell} A_\ell^m B_\ell^{m*}}{S_A(\ell) S_B(\ell)}, \quad (1.5)$$

where  $C_A^B(\ell)$  is the correlation of model B with A as a reference,  $S_A(\ell)$  and  $S_B(\ell)$  are the spectral amplitudes (square root of Eq. 1.4) of models A and B, respectively, and  $A_\ell^m$  and  $B_\ell^m$  are the spherical harmonic coefficients of models A and B, respectively. Examples of such comparisons are presented in Debayle and Ricard (2012) and Lekić and Romanowicz (2011a). A more quantitative analysis of this form was undertaken by Becker and Boschi (2002), with tomographic and geodynamic models correlated as a function of depth and harmonic degree.

A new method of qualitative analysis of tomographic models was proposed by Lekić and Romanowicz (2011b), who performed cluster analysis to identify several types of regions of the Earth with shear-speed profiles in the lithosphere–asthenosphere depth range similar within each. Such cluster analysis has been used in various applications for many years; in global seismology, its use was previously limited to the analysis of time-series data sets (Houser et al. 2008). The clusters, sharing similar  $V_S$  profiles, were selected using an objective criteria without any *a priori* information. Such cluster-based regionalization of tomographic models provides not only a novel means of classifying and characterizing the upper mantle structure identified by an individual model, but also is readily extended to the comparison of the prominent features of different tomographic models, as carried out by Lekić and Romanowicz (2011b) for the models SEMum (Lekić and Romanowicz 2011a), SAW24B16 (Mégnin and Romanowicz 2000), and S362ANI (Kustowski et al. 2008).

We perform regionalization of our model SL2013sv following the procedure of Lekić and Romanowicz (2011b). We resample the tomographic model into 1D shear-speed profiles, sampled every 10 km with depth between 30 and 350 km, and on a finer lateral grid than the original model, to avoid spatial aliasing. The triangular grid provides knots with approximately equal areas, ensuring that the polar regions are not over-represented as would occur in an un-weighted global cartesian grid. The clustering analysis is carried out using the MATLAB implementation of the *k-means* algorithm. Given a set of  $N$  observations  $\mathbf{x}_p$ ,  $(\mathbf{x}_1, \mathbf{x}_2, \dots, \mathbf{x}_N)$ , we wish to sort them into  $k$  sets  $[S_1, S_2, \dots, S_k]$  with corresponding centroids  $[\mathbf{m}_1, \mathbf{m}_2, \dots, \mathbf{m}_k]$ . The basic algorithm operates in two steps. First, the Euclidean distance between an  $\mathbf{x}_p$  and each  $\mathbf{m}_i$  is computed, with  $\mathbf{x}_p$  assigned to only one  $S_i$  with the minimum sum of squares:

$$S_i^{(t)} = \left[ \mathbf{x}_p : \left\| \mathbf{x}_p - \mathbf{m}_i^{(t)} \right\|^2 \leq \left\| \mathbf{x}_p - \mathbf{m}_j^{(t)} \right\|^2 \quad \forall \ 1 \leq j \leq k \right], \quad (1.6)$$

In the first iteration ( $t = 0$ ), the initial centroids  $\mathbf{m}_i^{(0)}$  are selected using a random subset of observations. In the second step, new centroids  $\mathbf{m}_i^{(t+1)}$  are computed based on the distribution of observations  $\mathbf{x}_p$  in each  $S_i$ :

$$\mathbf{m}_i^{(t+1)} = \frac{1}{|S_i^{(t)}|} \sum_{\mathbf{x}_j \in S_i^{(t)}} \mathbf{x}_j \quad (1.7)$$

This two step process is repeated until the assignments of  $\mathbf{x}_p$  into  $S_i$  no longer change.

In our case, the  $N$  shear-speed profiles (the  $\mathbf{x}_p$ , with  $p = 1, \dots, N$ ) are partitioned into  $k$  arbitrary sets such that each intra-cluster variance is minimized. We stress that all the cluster types and their geographic distribution are not predetermined, but result directly from the minimization. In particular, oceans and continents are not separated from each other *a priori* but fall into different clusters naturally. (We select  $k = 6$  and use 5 replicates in part to ensure consistent comparison with the results of Lekić and Romanowicz (2011b).

The results of the clustering of SL2013sv are shown in Fig. 1.8. The six clusters are readily distinguished: young oceans, ridges, and backarcs (which we label O1, identified with red); intermediate-aged oceans (O2, orange); oldest oceanic (O3, brown); continental regions presently deforming or having undergone deformation during the Phanerozoic (C1, light blue grey); stable continental regions of Precambrian fold belts and cratons modified in the Proterozoic (C2, blue); and stable Archean cratons (C3, green). The areas of the clusters are given in Table 1.1, along with their per cent coverage of the Earth's surface, for both SL2013sv and SEMum.

The three “ocean” clusters make up ~67 % of the Earth’s surface area. Locations that belong to the slowest cluster (O1, red) are predominantly beneath MORs and backarc basins. Along most MOR segments, the width of the cluster is not constant, but depends on the spreading rate and is confined to within ~2.0 Ma of the ridge axis. This cluster also includes several continental locations, including south-western North America, the northern portion of the East African Rift, the region including the Red Sea, the Dead Sea Transform and the East Anatolian Fault regions, the Pannonian Basin, and localized points in close proximity to known continental intra-plate volcanism. On its own, this cluster takes up almost 20 % of the Earth’s surface, with much of it over the East Pacific Rise and surroundings.

The cluster O3 (brown) includes the oldest oceanic regions. It is characterized by very high velocities in the uppermost mantle and makes up ~21 % of the Earth’s surface area.

The intermediate-age oceanic cluster (O2, orange) has the largest single surface area of all clusters, encompassing more than 26 % of the Earth’s surface.

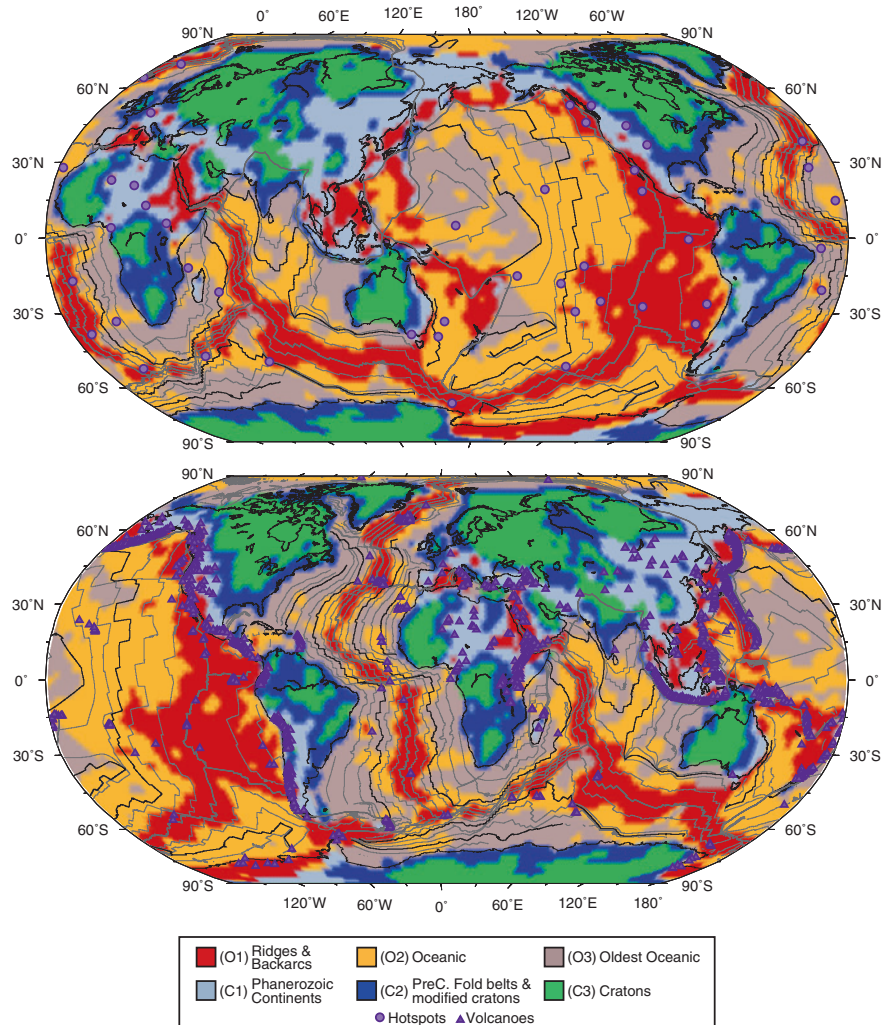


**Fig. 1.8** Tectonic regionalization of the Earth. The regionalization was computed from the model SL2013sv using the *k*-means clustering (Lekić et al. 2010). The classification and colour of each region are given in the legend. The two maps present the same data, with the difference that the top one is centred at 150°E and the bottom one is centred at 5°E. Known hot spots (Steinberger 2000) are plotted as purple circles (top) and volcanoes from the Smithsonian Global Volcanism database (Siebert and Simkin 2002) as purple triangles (bottom). Ocean-age contours (Muller et al. 1997) are indicated every 20 Ma (thin light grey lines) and 60 Ma (thin darker grey lines)

Of particular interest is the signature of lithospheric rejuvenation. This is evident along the Hawaiian and Emperor Islands hot spot track. Stretching to the northwest from Hawaii, a band of this cluster bisects through that of older oceanic lithosphere (O3) parallel with the string of islands. The variations in plate age do not

**Table 1.1** Summarizing the areal extent of the 6 different cluster types identified by the *k-means* algorithm applied to SL2013sv and SEMum

Region name	Cluster ID	Colour	SL2013sv SA		SEMum SA	
			km <sup>2</sup>	%	km <sup>2</sup>	%
Ridges and backarcs	O1	Red	$9.71 \times 10^7$	19.09	$1.10 \times 10^8$	21.55
Intermediate oceans	O2	Orange	$1.36 \times 10^8$	26.82	$8.80 \times 10^7$	17.28
Oldest oceanic	O3	Brown	$1.09 \times 10^8$	21.41	$1.31 \times 10^8$	25.83
Phanerozoic continents	C1	Light grey	$5.60 \times 10^7$	11.00	$6.71 \times 10^7$	13.18
PreCambrian fold belts and modified cratons	C2	Blue	$5.36 \times 10^7$	10.53	$7.18 \times 10^7$	14.10
Cratons	C3	Green	$5.77 \times 10^7$	11.33	$4.20 \times 10^7$	8.25

explain this pattern; the lithospheres to the west and east of this band are older and younger, respectively. Therefore, this band of oceanic lithosphere classified as “younger” than the surrounding lithosphere represents the lasting imprint due to the passage over the hot spot, which has rejuvenated the lithosphere, leaving a velocity structure more characteristic of a younger oceanic lithosphere.

A similar feature can be seen off the western margin of Africa. The Cameroon Line volcanic belt bisects the African continent, separating the west African craton from the Congo craton. The present locus of the volcanism (and possibly a hot spot, according to the Steinberger (2000) catalog) is indicated on the bottom (and the top) maps in Fig. 1.8, respectively. Extending south-westwards into the Atlantic Ocean towards the MOR is a thin band of oceanic lithosphere clustered as type O2, which cuts through type O3, old eastern Atlantic lithosphere. Further south, a similar band of O2 lithosphere may be associated with several hot spots in the south Atlantic (Tristan and Verna).

Continents are characterized by the other three cluster types. The cluster with the highest shear speeds includes the cratons (C3, green). It makes up 11 % of the Earth’s surface area and includes all the major and minor Archean cratons making up the continental cores. In addition to the large cratons within each of the continents, we also map smaller cratonic blocks, such as the Sichuan block within the Yangtze craton. In the African continent, each of the three main cratons is clearly identified. Great improvement compared to previous tomographic models can be seen in South America, where the three main cratons are mapped clearly: the large Amazonia in the north east; the south-eastern Río de la Plata and eastern central São Francisco, together.

Somewhat lower shear speeds characterize the cluster that includes Precambrian fold belts and modified cratons (C2, blue). This cluster takes up the smallest proportion of the Earth’s surface, at just over 10 % of surface area. Tectonic units that fall within it often occupy the spaces between Archean cratons, for example, in South America, southern Africa, and in the West Siberian platform between the east European and Siberian cratons.

The last cluster includes predominantly Phanerozoic portions of the continents (C1, light grey) and makes up just over 11 % of the Earth's surface. It is characterized by seismic-velocity profiles slower than those of the stable continental regions. It is observed stretching along the entire western margin of North America, from the Aleutians and Alaska southwards through the Canadian and US Cordillera into Mexico and Central America. A similar band of C1 can be seen in the Cordillera of South America and extending southwards through the Antarctic Peninsula. It is also dominant across much of East Asia and extends through the Zagros Mountains and Anatolia to the Alps and Iberia. Finally, it is prevalent in much of north-central Africa. There and elsewhere, the portions of continents that have thin, warm lithosphere and comprise the cluster C1 include almost all the locations of intra-plate continental volcanism (purple triangles, Fig. 1.8), as shown previously for Europe by Legendre et al. (2012).

In Fig. 1.9, we compare different tectonic regionalizations. Two of them were computed from surface-wave tomographic models, with no *a priori* information. The other three, GTR1 (Jordan 1981), RUM (Gudmundsson and Sambridge 1998), and 3SMAC (Nataf and Ricard 1996), were constructed using compilations of *a priori* geologic and geophysical information. The SEMum clusters are exactly those from Lekić and Romanowicz (2011b), obtained directly from the authors.

The regionalizations based solely on tomography (left panel) have strong similarities at large scales. The biggest difference between SL2013sv and SEMum is the relative partitioning of the oceanic clusters. In SEMum, the O2 cluster is reduced in area by >9 %, whereas O1 and O3 increase by 2.5 and 4.5 %, respectively. Lekić and Romanowicz (2011b) suggest that the presence of plate-motion-aligned “finger-like” structures in the O2 cluster is associated with small-scale convection cells known as Richter Rolls, previously inferred in the Pacific from gravity measurements. Similar fingers are not observed in the clustering of SL2013sv; however, as pointed out above, a section of the O2 cluster following both the Hawaiian and Emperor Islands hot spot tracks and that associated with the Cameroon Line volcanic belt bisects two regions of O3, suggesting a lasting imprint in the oceanic lithosphere due to rejuvenation by an impinging hot spot. The ridge cluster (O1) is very similar between SL2013sv and SEMum, with those in the former being slightly narrower at many ridge segments. Additionally, much of the tectonically active western USA is classified as O1 (young ocean) in SEMum, whereas in SL2013sv, most of this region is instead classified as C1 (tectonic continent), with O1 seen only in close proximity to the rifting and spreading within the Gulf of California.

In the right hand panels of Fig. 1.9, we also include the regionalizations based on *a priori* information: GTR1, RUM, and 3SMAC. Note that for 3SMAC, we only plot the continental regions. We briefly highlight several key differences between the regionalizations based on *a priori* information and on tomography. First, in the *a priori* models, Australia is made up of cratons in the west and a

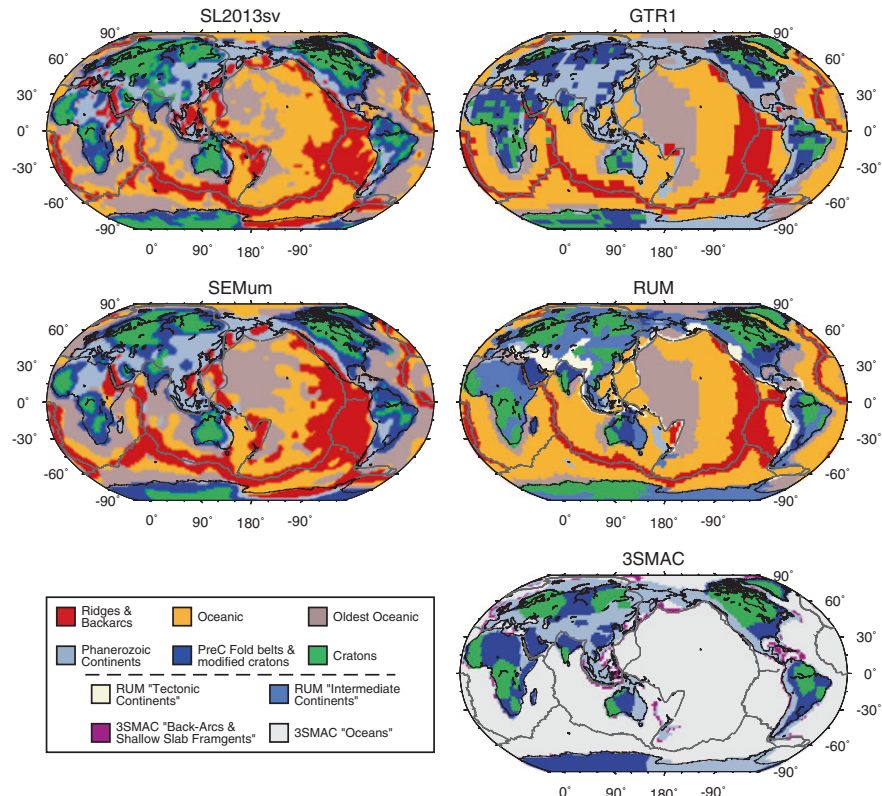


**Fig. 1.9** Comparison of tectonic regionalization for the multimode surface wave tomography models SL2013sv (Schaeffer and Lebedev 2013) and SEMum (Lekić and Romanowicz 2011a) with the a priori models 3SMAC (Nataf and Ricard 1996), RUM (Gudmundsson and Sambrook 1998), and GTR1 (Jordan 1981). The results for SEMum were obtained directly from the authors. The same colours for the six *k-means* clusters (from Fig. 1.8) are shown in the legend. The additional colours for 3SMAC and RUM (which have 8 and 9 cluster types, respectively) are also indicated. Note that for the RUM model, our current classification of “Phanerozoic Continents (C1)” is equivalent to the RUM “Young Continent”, “Precambrian fold belts and modified cratons (C2)” are equivalent to RUM “Old Continent”, and “Cratons (C3)” match the RUM “Ancient Continents”. (The tectonic regionalization plotted for 3SMAC is as in the 3SMAC model distribution, which sets all the oceans to the same type, although regionalization of oceans based on their age is implied.)

platform type in the centre; in tomography-based regionalizations, the fast and deep cratonic root is imaged to occupy most of central Australia, extending almost to the coast in the west, into the Arafura and Timor Seas to the north, and much further eastward across the continent. Second, the tomography-based regionalizations identify relatively larger proportions of ancient oceanic (O3) clusters.

Outside of the Pacific Ocean, *a priori* models identify relatively little O3 (old ocean) lithosphere. The tomography models, in contrast, consistently identify such lithosphere in the other oceans, including the Atlantic (off the coasts of North and South America and Africa) and Indian (eastern Africa and west of Sumatra and Australia) Oceans.

## 1.5 1D Shear-Speed Profiles of the Upper Mantle

To look at the global distribution of shear velocities from yet another perspective, we have extracted a 1D absolute velocity profile from each of the model knots of SL2013sv (7842 locations). All of these profiles are plotted together in each of the panels of Fig. 1.10. The minimum/maximun velocity envelope is indicated by the light-blue shading. The shear-speed profiles are binned, with the relative density of profiles at each depth and each speed value indicated by colour, with blues indicating minimal and warmer colours through to black indicating increasing sampling. Superimposed are the centroids of the clusters given by the empirical tectonic

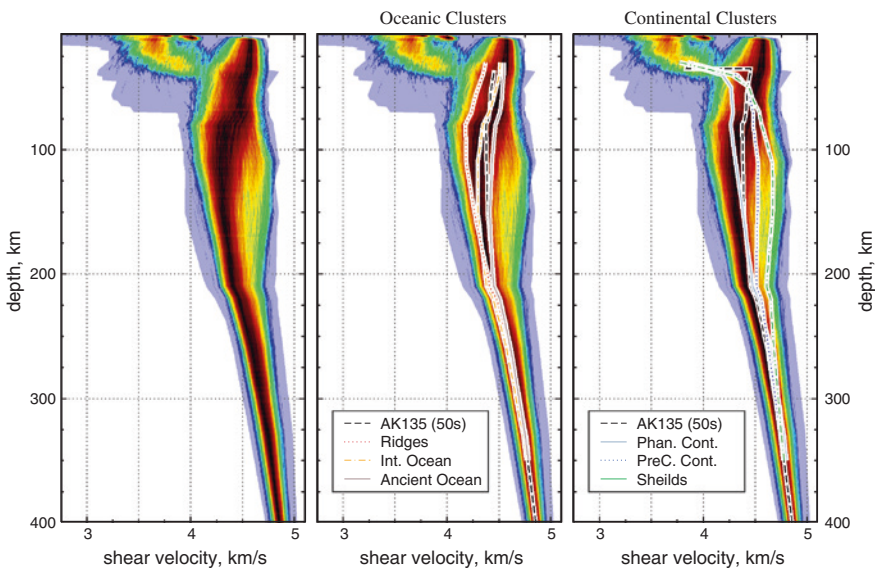


**Fig. 1.10** Global variability in 1D shear-wave speed profiles in the crust and upper mantle. The 1D profiles beneath the 7842 model knots of the model SL2013sv, distributed on the sphere with approximately equal spacing, are binned. The relative density of profiles at each depth and each shear-speed value is shown by colour, with *blues* indicating minimal sampling and warmer colours through to *black* indicating increasing sampling. The minimum/maximun velocity envelope is indicated by the *light-blue shading*. The *centre panel* has the cluster centroids associated with oceanic lithosphere plotted, whereas the *right panel* indicates those for clusters associated with continental regions. These centroid profiles were generated for the depth range 30–350 km

regionalization: the oceanic ones (O1–O3) in the centre panel and the continental ones (C1–C3) in the right panel. In the centre and right panels, the mantle reference model (AK135, recomputed at 50 s reference period) is also plotted, with the dashed black line.

The strongest heterogeneity in the oceans (Fig. 1.10, middle panel) is confined to the upper 200 km of the mantle. At 30–50 km depths, the O2 and O3 clusters are quite similar and correspond with the most densely sampled velocities (darkest colours). With increasing depth, these two clusters diverge, with the oldest oceanic type remaining the fastest down to 200 km depth. In regions associated with ridges and backarcs (O1), the lowest velocity anomaly occurs in the depth range 80–115 km and lies at the slower (left) side of the most densely sampled region (reds and blacks). Wave speeds within this cluster converge with those of the middle-aged oceans cluster (O2) at a depth of 150 km. The cooling of oceanic upper mantle with the age of the plate is fast at shallow depths (wave speeds beneath the middle-aged oceans nearly reach old-oceans values in the shallow mantle) and eventually affects the top 200 km of the mantle. Beneath 200 km depth, all three profiles are nearly indistinguishable.

The continental profiles (C1–C3) are dominated by two distinct patterns. As expected, stable continental interiors (C2 and C3) show mantle velocities much faster than the reference, typical of cratonic and stable-continent environments. In contrast, the C1 cluster associated with Phanerozoic portions of continents (recent or active continental deformation) is characterized by an uppermost mantle slower than the reference, down to depths of 150 km. The C3 cluster demonstrates the typically high-velocity lithospheric root characteristic of cratonic regions; the high velocities persist to a depth of ~250 km, before converging with the reference velocity. In comparison, the velocity of the Precambrian fold belts and modified cratons (C2) approaches the reference at a shallower depth of ~200 km. Although the C3 cluster remains faster than C2 to approximately 250–275 km depth, we consider the base of the continental lithosphere to occur closer to 200 km depth, beneath which the relative velocity perturbation with respect to surrounding continental regions is substantially reduced.

We can also examine shear-wave velocity distribution in the shallow mantle (<30 km depth), which is not included in the clustering analysis (the clusters become dominated by the strong variations in crustal structure instead of the lithospheric mantle). In the depth range 10–30 km, the sampling has a bi-modal distribution, with a broad slow region representative of continental crust, and a narrower fast region indicative of the uppermost oceanic lithosphere. Since the knots of the model grid represent roughly equal areas, the entire globe is sampled uniformly, contrary to the observations made for the fundamental-mode group-velocity distribution, where sampling at the shortest periods was influenced by the distributions of sources and stations.

In Fig. 1.11, we plot histograms of shear velocity at ten different depths in the crust, upper mantle, and transition zone; these represent cross sections through the binned profiles of Fig. 1.10. It is clear that the strongest shear-wave speed heterogeneity is largely at depths less than ~300–350 km. (For this comparison, each

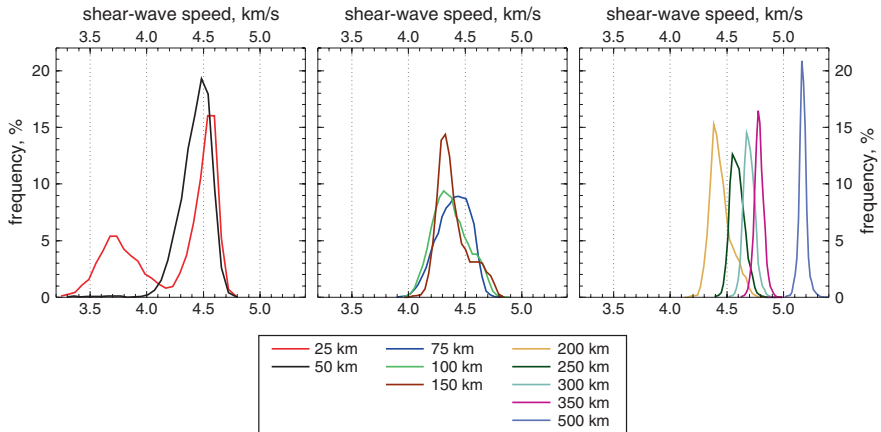


**Fig. 1.11** Histograms of global shear-wave speed distributions at different depths within the Earth's crust and upper mantle. Each histogram was computed over all 7482 horizontal shell knots in the model SL2013sv and with the same number of bins (so that the bin width decreases with depth)

histogram was computed with the same number of bins, so that the bin width decreases with depth.)

The 25 km histogram shows a bi-modal distribution of velocity, already mentioned above, with a broad band of lower velocities centred at  $\sim 3.7 \text{ km s}^{-1}$  and a second much narrower region at  $\sim 4.6 \text{ km s}^{-1}$ . These represent the continental crust and oceanic mantle, respectively. The centre of each histogram (highest rate of occurrence) shifts to lower velocity from 25 to 100 km depth, before beginning to move to higher velocities at 150 km depth. At 150 and 200 km depth, the tails of the distributions extend to velocities up to  $\sim 350\text{--}500 \text{ m s}^{-1}$  higher than that at the distribution maximum, due to the high-velocity anomalies within the deep lithospheric roots of cratons; at 250 km, this high-velocity tail is nearly gone. With increasing depths (300–500 km), the central velocity increases and the distributions look much more Gaussian, with standard deviation decreasing.

## 1.6 Comparison of Recent Global Models

Much of our current understanding of the large-scale heterogeneity in deep Earth structure has come from the analysis of global tomographic models. Each model is constructed using different data sets, data types, and methodologies. Body-wave travel-time tomography, for example, is very effective for high-resolution imaging of subduction zones, due to the high density of crossing rays given by the stations and number of events in these regions (e.g. Bijwaard et al. 1998; Karason and van der Hilst 2001; Grand 2002; Montelli et al. 2004; Amaru 2006; Li et al.

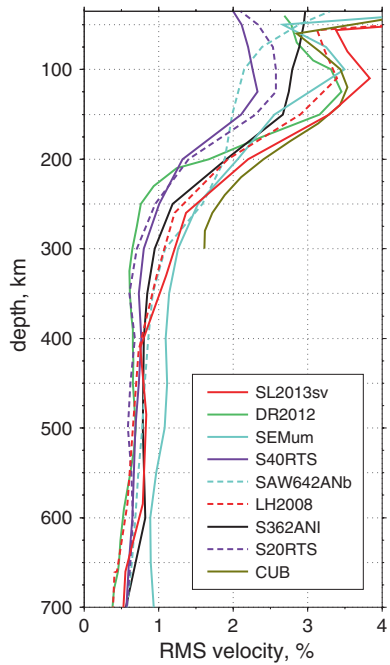
2008; Simmons et al. 2012). However, global body-wave tomography models tend to lack resolution in the lithospheric mantle in regions where seismicity and station coverage are sparse or absent.

Surface-wave models are constrained by the waves that propagate along the Earth's surface through the crust and upper mantle and can recover the shear-velocity structure in the lithosphere–asthenosphere depth range globally, with relatively uniform resolution. The addition of multimode  $S$  waves (higher mode surface waves make up  $S$  and multiple  $S$  waves) augments the fundamental-mode sensitivity to constrain structure at depths down to the base of the transition zone (see Fig. 1.1). Important insights into the structure of deep lithospheric roots of continental cratons and the structure and evolution of oceanic lithosphere have been obtained from models constrained with surface waves (e.g. Montagner and Tanimoto 1991; Zhang and Tanimoto 1993; Boschi and Ekström 2002; Shapiro and Ritzwoller 2002; Zhou et al. 2006; Nettles and Dziewónski 2008; Ekström 2011) and surface waves combined with body waves (or fundamental and higher modes, e.g. Woodhouse and Dziewónski 1984; Li and Romanowicz 1996; Mégnin and Romanowicz 2000; Debayle et al. 2005; Panning and Romanowicz 2006; Lebedev and van der Hilst 2008; Ferreira et al. 2010; Panning et al. 2010; Lekić and Romanowicz 2011a; Debayle and Ricard 2012; Schaeffer and Lebedev 2013). A number of surface-wave models have also been computed with teleseismic travel times and normal mode splitting functions incorporated into the data sets (e.g. Su et al. 1994; Masters et al. 1996; Ritsema et al. 1999; Masters et al. 2000; Gu et al. 2001; Ritsema et al. 2004; Houser et al. 2008; Kustowski et al. 2008; Ritsema et al. 2011).

In addition to the data sensitivities and basic methodologies, properties of each tomographic model also depend on its regularization (damping, smoothing), chosen by its creators. A comparison of a range of different models reveals the features that are resolved and confirmed by most. In addition, this helps establish the comparative advantages of different models. In this section, we compare SL2013sv with eight other global tomography models: DR2012 (Debayle and Ricard 2012), SEMum (Lekić and Romanowicz 2011a), S40RTS (Ritsema et al. 2011), SAW642ANb Panning et al. (2010), LH2008 (Lebedev and van der Hilst 2008), S362ANI (Kustowski et al. 2008), S20RTS (Ritsema et al. 1999, 2004), and CUB (Shapiro and Ritzwoller 2002). Each of these models is parameterized differently and is constrained by a different data set, with different sensitivity to upper mantle structure.

SEMum is a Voigt-average shear speed and radial anisotropy model,  $V_S^2 = \frac{1}{3}(2V_{SV}^2 + V_{SH}^2)$  (Babuska and Cara 1991) and  $\xi = V_{SH}^2/V_{SV}^2$ , respectively, constrained by long-period waveforms (multimode Rayleigh and Love waves and long-period body waves) and group-velocity dispersion maps; SAW642ANb is derived from a similar data set. The CUB model (CU\_SDT1.0) is an isotropic shear-velocity and radial anisotropy model of the crust and uppermost mantle derived from fundamental-mode Rayleigh and Love group and phase measurements. LH2008 is a predecessor of the SL2013sv model generated using the same methodology but constrained by fewer seismograms and computed with lower target resolution. S362ANI is a Voigt-average whole-mantle isotropic shear-velocity

**Fig. 1.12** Root mean square (RMS) of shear-wave speed variations in the upper mantle, according to selected models of the last decade: SL2013sv (Schaeffer and Lebedev 2013), DR2012 (Debayle and Ricard 2012), SEMum (Lekić and Romanowicz 2011a), S40RTS (Ritsema et al. 2011), SAW642ANb (Panning et al. 2010), LH2008 (Lebedev and van der Hilst 2008), S362ANI (Kustowski et al. 2008), S20RTS (Ritsema et al. 1999, 2004), and CUB (Shapiro and Ritzwoller 2002)



model generated from surface-wave dispersion measurements, mantle and body-wave waveforms, and body-wave traveltimes. S40RTS (and S20RTS) are isotropic shear-velocity models of the mantle constrained by three data sets: minor and major arc Rayleigh wave dispersion, teleseismic body-wave traveltimes, and spheroidal-mode splitting functions; S40RTS is a newer model constructed with more data. Finally, DR2012 is an upper-mantle  $S_V$ -wave model constrained by multi-mode Rayleigh waveforms.

In Figs. 1.12, 1.13, 1.14, 1.15, 1.16, 1.17, 1.18, and 1.19, we perform a consistent comparison of the models. We re-sample each to the same  $0.5^\circ$  latitude–longitude grid and extract or compute only the  $V_{SV}$  component for comparison. At each depth for each model, the mean value (computed as a weighted average using the cell areas) is removed. Where required, the grid values are converted to per cent variation from this mean. We first compare the root-mean-square (RMS) velocity perturbations of each model as a function of depth and then compare map views at different depths in the crust and upper mantle.

### 1.6.1 RMS of Shear-Wave Speed Perturbations

The RMS of wave speed perturbations as a function of depth provides a simple statistical measure of the magnitude of anomalies in each model. For each model, a weighted RMS is computed as follows:

$$\langle x_i \rangle = \sqrt{\frac{\sum_{j=1}^N (x_{ij} - \bar{x}_i)^2 w_j}{\sum w_j}}, \quad (1.8)$$

where  $\langle x_i \rangle$  is the RMS at the  $i$ th depth,  $x_{ij}$  is the model perturbation at the  $j$ th grid cell (at depth  $i$ ),  $w_j$  is the area of each cell (the same at each depth),  $N$  is the number of horizontal cells (the same at each depth), and  $\bar{x}_i = \sum (x_{ij} w_j) / \sum w_j$  is the mean value at the given depth. As the mean has already been removed ( $\bar{x}_i = 0$ ), the RMS reduces to:

$$\langle x_i \rangle = \sqrt{\frac{\sum (x_{ij})^2 w_j}{\sum w_j}}. \quad (1.9)$$

In Fig. 1.12, the RMS calculated using Eq. 1.9 for each of the nine models is plotted as a function of depth over the upper mantle and transition zone depth range. For all models, the RMS reaches a mantle maximum at a depth of less than 150 km, most commonly between 100 and 130 km. Between 150 and 300 km depths, the RMS drops off rapidly, to  $\sim 1\%$  at 300 km. Through the rest of the upper mantle and transition zone, this gradually decreases to an average value of  $\sim 0.6\%$ . At the shallowest depths (i.e.  $\sim 50$  km and less), SL2013sv, LH2008, and CUB have the highest RMS, which reflects their recovery of the global crustal structure (although not obvious, SEMum's RMS also increases at similar shallow depths). The other models use different methods of crustal corrections (aimed at isolating and removing the effect of the crust and focussing on the mantle only) and do not resolve crustal structure.

In the upper 200 km, SL2013sv shows close to the highest RMS, indicative of greater structural heterogeneity in it compared to other models; SEMum, CUB, DR2012, and LH2008 attain RMS values close to that of SL2013sv. At 125 km, these five models have an average RMS of 3.4 %, whereas S40RTS, S20RTS, and SAW642ANb have an average of 2.3 %. Based on this difference, these two groups can be separated into two classes of models: the latter is a “lower amplitude” class, whereas the former represents a “higher amplitude” class. The model S362ANI falls between these two classes, with an RMS of 2.75 %.

From the 100–150 km depths to just above the transition zone, the RMS of the models drops by a factor of 2–3, with the bulk of this decrease taking place between 150 and 300 km depths. The CUB model RMS becomes higher than that of all other models in the mid-upper-mantle depth range. However, we do not plot it to depths greater than 300 km, as its uncertainty estimates identify robust

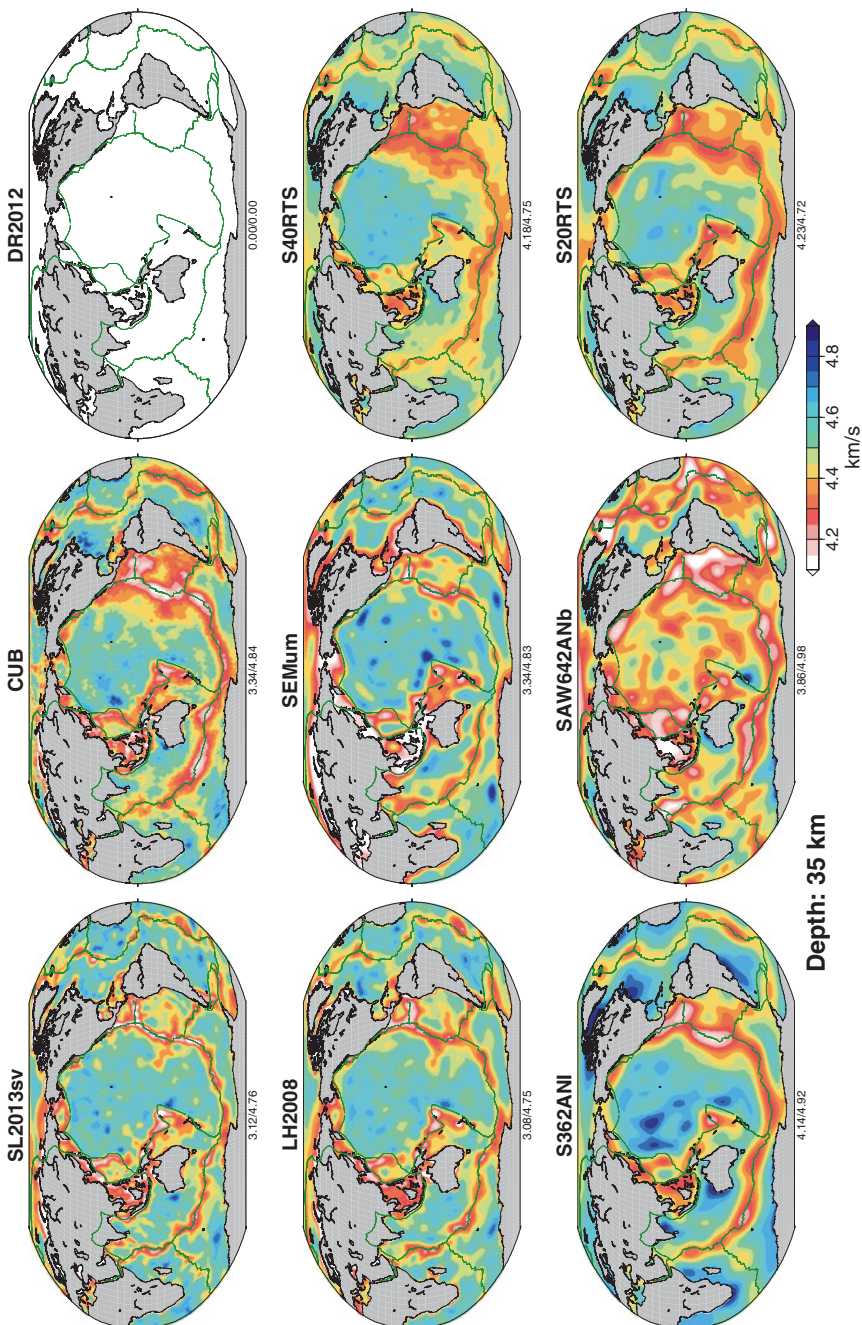


**Fig. 1.13** Comparison of SL2013sv and eight other global tomographic models at a depth of 35 km. The models are as follows: DR2012 (Debayle and Ricard 2012), SEMum (Lekić and Romanowicz 2011a), S40RTS (Ritsema et al. 2011), SAW642ANb (Panning et al. 2010), LH2008 (Lebedev and van der Hilst 2008), S362ANI (Kustowski et al. 2008), S20RTS (Ritsema et al. 1999, 2004), and CUB (Shapiro and Ritzwoller 2002). The absolute velocity ( $V_{\text{SV}}$ ) of each model is plotted, with the colour scale saturating for velocities less than  $4.1 \text{ km s}^{-1}$  to highlight structure in the mantle instead of the crust. Continental regions were *greyed out* to focus the comparison on the oceanic mantle, as the continental crust was not meant to be resolved accurately in some of these models (a 36 km cross section through SL2013sv, which does resolve anomalies in the continental crust, relative to a 3D reference model, is plotted in Fig. 1.3). Each models' global minimum and maximum absolute velocity (over both continents and oceans) is indicated beneath the maps, and the same linear colour scale is used in each

features persisting only to a depth of  $\sim 250$  km (Shapiro and Ritzwoller 2002). The RMS of the model DR2012 decreases most rapidly in this depth range and has the smallest RMS by 225 km depth. SL2013sv, LH2008, SAW642ANb, and SEMum maintain an overall higher RMS to a depth of 400 km.

In the transition zone, seven of the eight remaining models (excluding SEMum) have very similar RMS values, with variations of around 15 % from the average RMS of 0.6 %. SL2013sv has an RMS in the middle of this range through most of the transition zone. SEMum stands out with a significantly higher RMS (on average  $\sim 1$  %) between 400 and 700 km; the high amplitudes that give rise to this increased RMS are clearly apparent in the SEMum model (Fig. 1.19 at 500 km depth).

## 1.6.2 Map View Comparisons

In Figs. 1.13, 1.14, 1.15, 1.16, 1.17, 1.18, and 1.19, we compare the shear-wave speed structure in the Earth's upper mantle as resolved by the nine recent global tomographic models constrained using data sets that included surface-wave measurements. The depths plotted are 35 km in Fig. 1.13, 50 km in Fig. 1.14, 100 km in Fig. 1.15, 150 km in Fig. 1.16, 250 km in Fig. 1.17, 350 km in Fig. 1.18, and 500 km in Fig. 1.19. Each model is re-sampled to the same  $0.5^\circ$  grid, colour scales are indicated (absolute or relative) at the lower right of each figure, and the total range for each model is indicated in small print beneath each map. For depths 50 km and greater, the mean absolute velocity of each model is removed, with perturbations plotted from this value in per cent. The location of the main plate boundaries is indicated by a thin green line. A model is plotted with no colours (DR2012 at 35 km and CUB at 350 and 500 km) when that depth is not included in the model files.

In a few of the models, the strong crustal heterogeneity in the Earth was accounted for through the use of “crustal corrections”, which remove the effects of a predetermined crustal model from the measurements (see Boschi and Ekström 2002; Gu et al. 2003; Chevrot and Zhao 2007; Kustowski et al. 2007; Marone

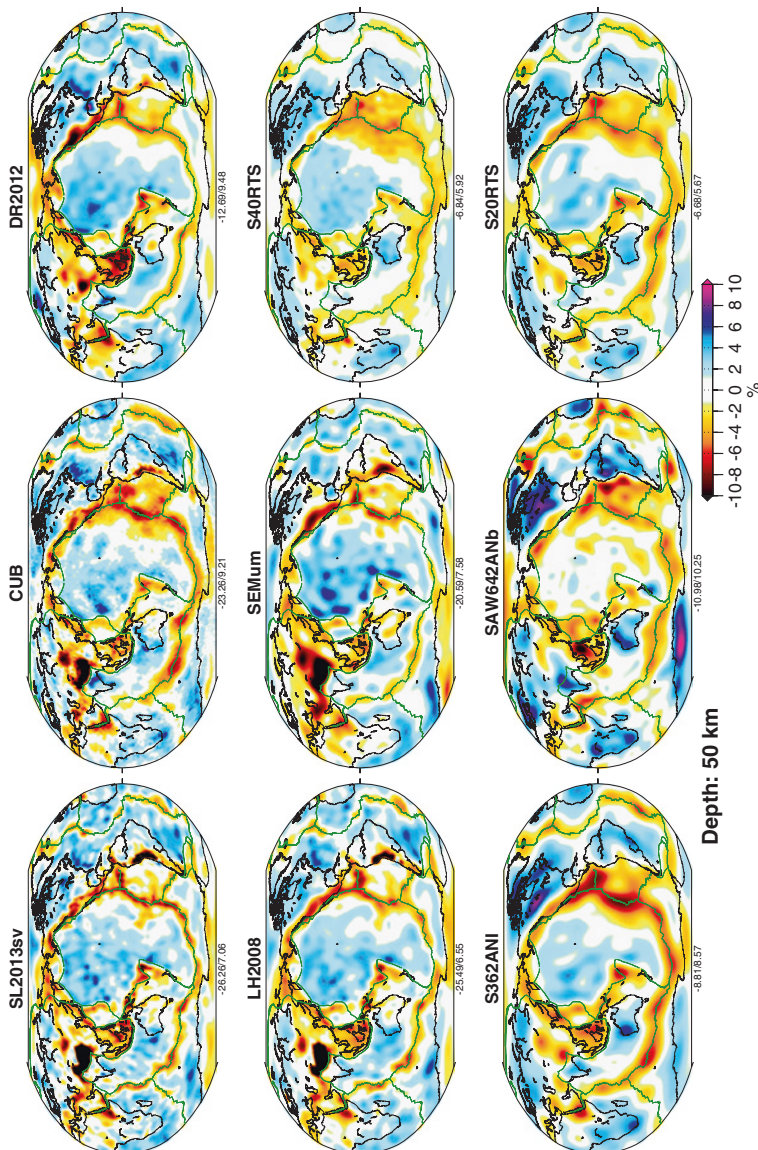


**Fig. 1.14** Comparison of SL2013sv and eight other global tomographic models at a depth of 50 km. Models are the same as those in Fig. 1.1. Perturbations are plotted in per cent with respect to the mean absolute velocity of each model. The minimum and maximum perturbations are indicated beneath the maps; the same linear colour scale is used for each map

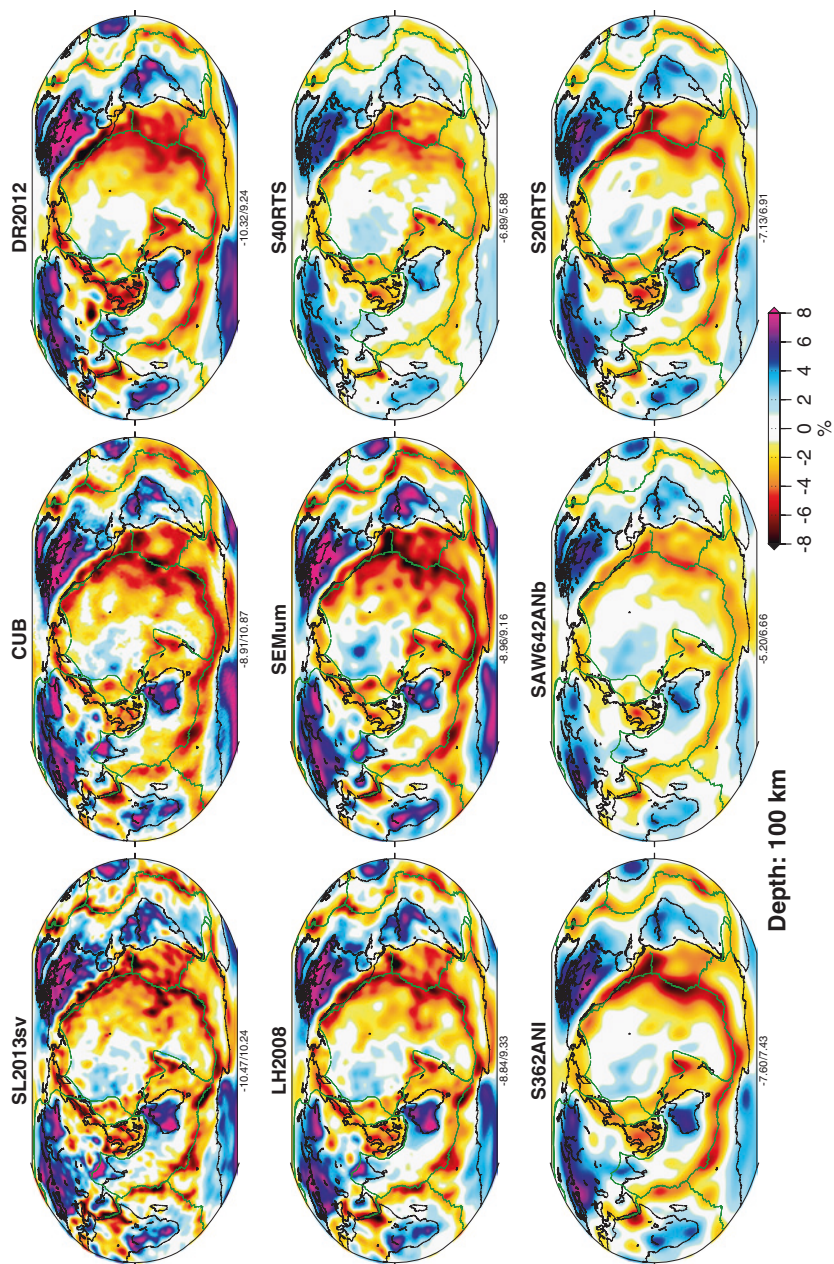
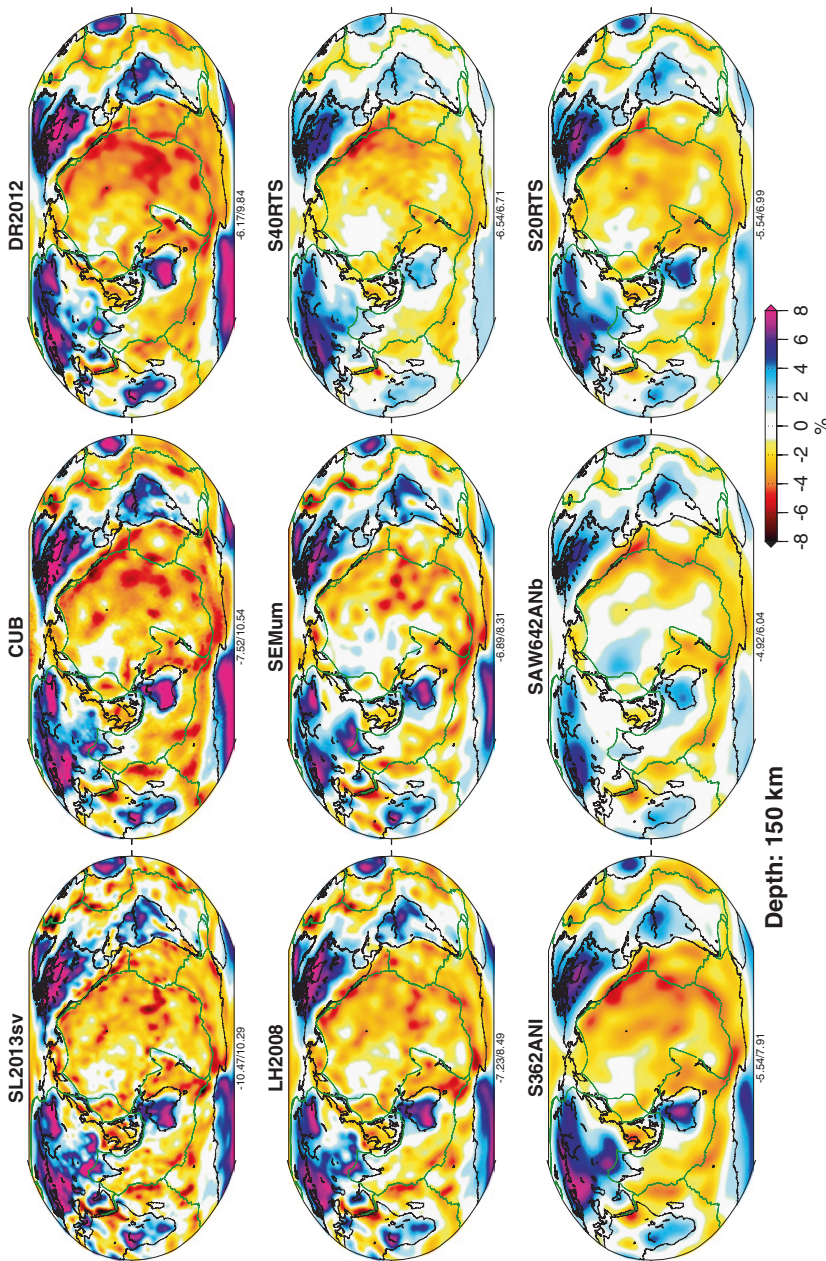


Fig. 1.15 Comparison of SL2013sv and eight other global tomographic models at a depth of 100 km depth. The models and plotting conventions are as in Fig. 1.14



**Fig. 1.16** Comparison of SL2013sv and eight other global tomographic models at a depth of 150 km depth. The models and plotting conventions are as in Fig. 1.14

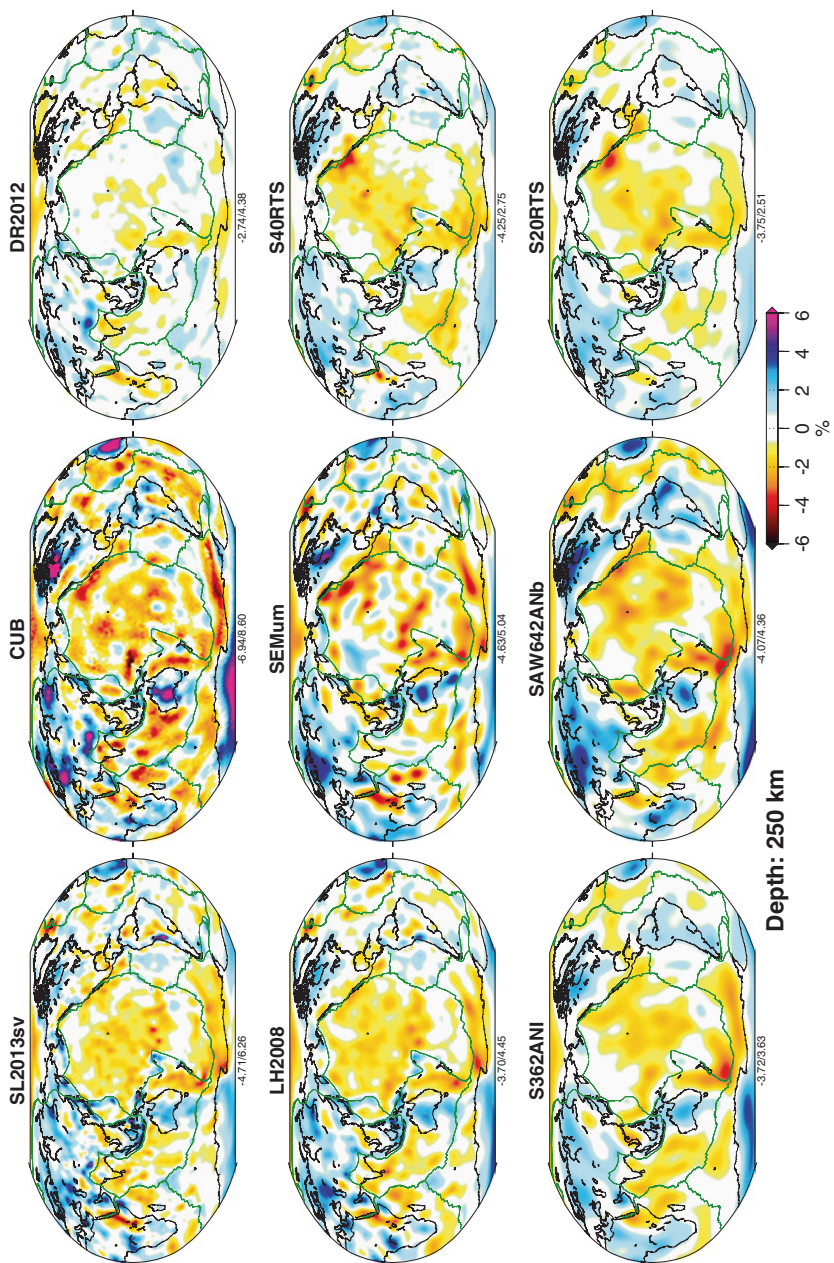
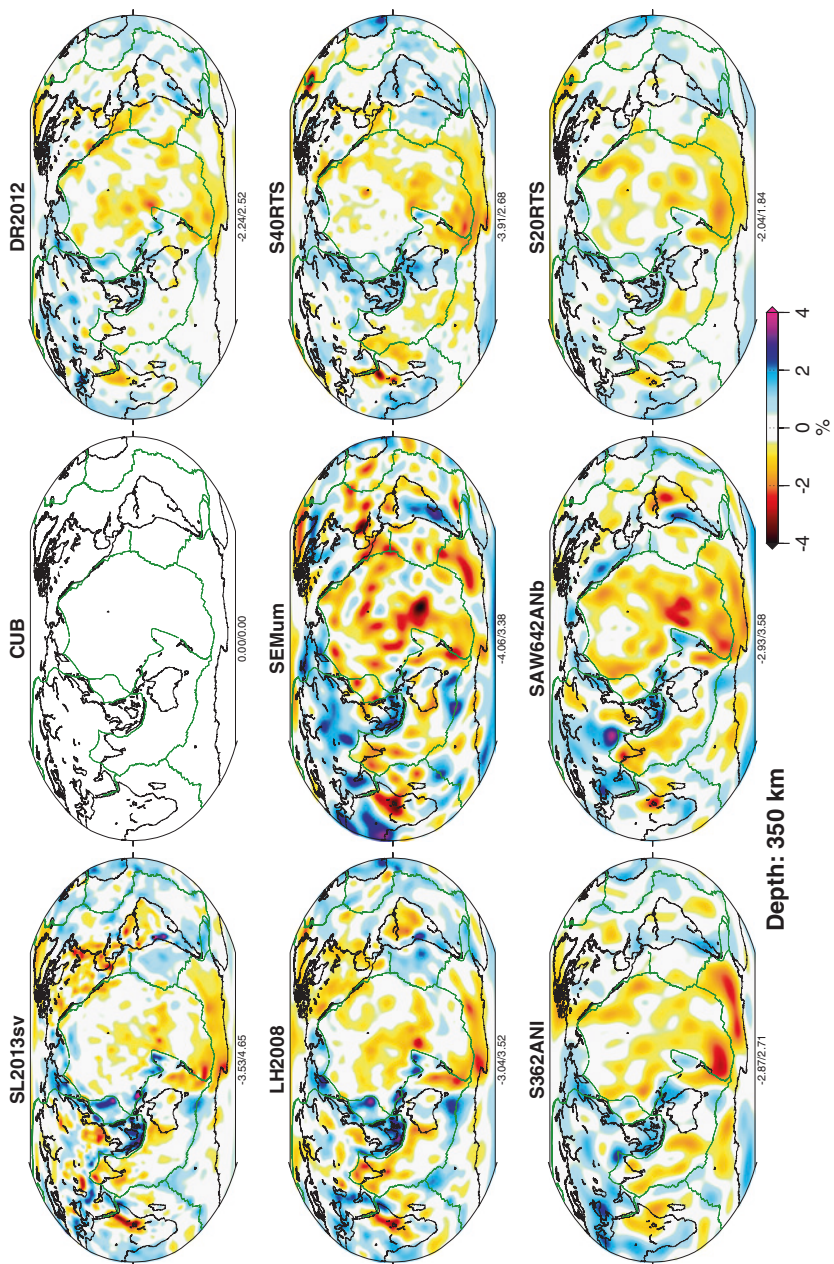


Fig. 1.17 Comparison of SL2013sv and eight other global tomographic models at a depth of 250 km depth. The models and plotting conventions are as in Fig. 1.14



**Fig. 1.18** Comparison of SL2013sv and eight other global tomographic models at a depth of 350 km depth. The models and plotting conventions are as in Fig. 1.14

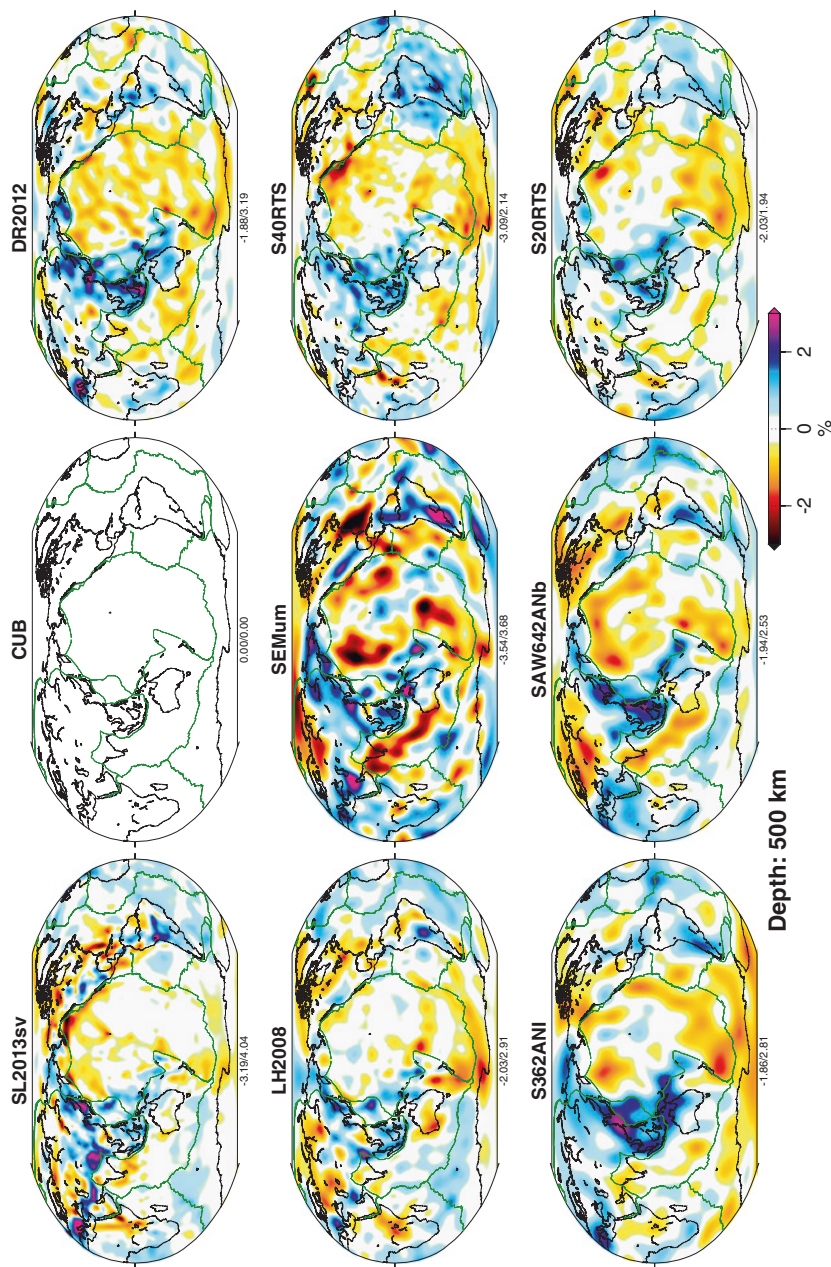


Fig. 1.19 Comparison of SL2013sv and eight other global tomographic models at a depth of 500 km depth. The models and plotting conventions are as in Fig. 1.14

and Romanowicz 2007; Bozdag and Trampert 2008; Lekić et al. 2010, for further information). As a result, it is not straightforward to interpret what the structure at crustal depths within these models represent. We plot a 35 km map view for 8 of the 9 models in Fig. 1.13 (shallowest knot of DR2012 is at 40 km) but focus on the uppermost mantle and, thus, grey-out the continents, with their Moho normally near to or below 35 km depth (we note that in many cases, the authors of the different models would not interpret the structures at these shallow depths). Although we do not intend to describe in detail the relative merits of the different approaches, we do summarize those of each model for insight into the comparisons. For details on the treatment of the crust in each model, we refer the interested reader to each of the model papers.

In S362ANI, the CRUST2 (Bassin et al. 2000) reference model is assumed as an *a priori* model. In S40RTS and S20RTS, crustal corrections were performed using CRUST2 and CRUST5.1 (Mooney et al. 1998), respectively. DR2012 uses a fixed crustal structure based on 3SMAC and solves for perturbations in regions where the Moho is shallower than 40, 50, and 70 km depth. The authors only show tomographic maps for depths larger than 100 km in order to avoid possible contamination by crustal structure; here, we include DR2012 at 50 km for completeness in the comparison. SAW642ANb utilizes a linear correction methodology (developed from Lekić et al. 2010) to account for crustal structure, which they demonstrate improves variance reduction compared to nonlinear corrections as used in SAW642AN (Panning and Romanowicz 2006). SEMum use a 3D, smoothly varying, 60-km-thick effective elastic medium as a crustal model, which is constrained by group-velocity dispersion data, such that the effective crust produces the same waveforms as a thinner layered crust. The CUB model uses a number of different inputs to constrain the crustal reference model, including various sediment thickness models, crustal thickness models (CRUST5.1 and maps from the Russian Institute of Physics of the Earth), as well as thickness estimates based on seismic profiles. Additionally, CUB includes crustal parameters in the inversion, which allows perturbations from the reference model to be determined.

In SL2013sv and LH2008, a 3D crustal reference model based on CRUST2 is used in both the waveform fitting and tomographic inversion (for more detail, see Schaeffer and Lebedev 2013; Lebedev and van der Hilst 2008; Lebedev et al. 2005). Perturbations from this crustal model are then *solved for* directly. In continental regions, three depths of the model grid knots (at 7, 20, and 36 km depth) often fall within the crust; in the oceans, this is normally limited to one knot at 7 km depth. Although CRUST2 is known to be imperfect at many locations, inclusion of the crustal knots into the inversion enable perturbations relative to the 3D reference to be determined in regions where the data require them. As a result, in addition to preventing artefacts at depth in the mantle due to unaccounted for or assumed crustal structure, a global crustal model is generated (beginning at a depth of 7 km). SL2013sv clearly recovers strong perturbations from the reference model that are required by the data; a prominent example of this is the Tibetan

Plateau, where boundaries of a strong low-velocity anomaly in the model follow closely the boundaries of the plateau at the surface (this is illustrated in Fig. 1.3).

To facilitate easier comparison of the shallowest structure in the different models (Fig. 1.13), we plot the absolute velocity variations in each of the models. However, to reduce the effect of the strongly varying crustal structure (and correction terms), the colour scale saturates to white for velocities less than  $4.1 \text{ km s}^{-1}$ , which emphasizes the mantle structure within each model (essentially the oceanic regions), and the continents have been coloured grey.

The degree of heterogeneity as observed in each of the nine models varies substantially at depths of 35 and 50 km depth (Figs. 1.13 and 1.14). The dominant features common between all models are the low-velocity anomalies associated with the spreading ridges, back arcs, and regions of continental deformation (at 50 km), as well as relatively high velocities in the uppermost oceanic lithosphere. SL2013sv recovers these features at a finer resolution. For instance, at both 35 and 50 km depth, the central low-velocity anomalies associated with the MORs are very tightly confined to the region around the ridge axis, for most of the ridge segments globally. Although this signature of MORs is observed in all models to varying degrees, the highest amplitude anomalies are not as continuous and extend much greater distances away from the spreading centre. Similarly, the very low-velocity anomaly associated with the partially molten Tibetan crust is observed in SEMum, CUB, SL2013sv, DR2012, and LH2008. However, the low-velocity anomaly in SL2013sv has a closer correlation with the regional tectonic boundaries. The northern boundary corresponds with the surface expression of the Altyn Tagh Fault; to the west, low velocities are also present in the Hindu Kush and Pamir Mountains; in the east, the low-velocity anomaly extends south-east around the eastern Himalayan syntaxis.

At a depth of 100 km (Fig. 1.15), the signature of the spreading centres is still one of the dominant features in all the models, although there remain variations in the width and resolution of the central anomaly underlying the ridge centre. At 150 km depth (Fig. 1.16), the strongest anomaly of the ridge is gone in all the models. Instead, most of the oceans now show a relatively uniform, low-velocity asthenosphere. Smaller-scale heterogeneities in the Pacific, Atlantic, and Indian Oceans remain in SEMum, CUB, SL2013sv, DR2012, and LH2008. A strong low-velocity anomaly remains beneath Iceland in SL2013sv, as well as in LH2008, CUB, and SEMum. In SL2013sv, the strong, well-defined anomaly here is seen down to 250–270 km depth (Figs. 1.4 and 1.17).

The 100–150 km map views are dominated by the strong positive anomalies associated with the stable lithospheric roots of cratons, which can be seen in each of the models beneath each of the continents. At shorter wavelengths (<500–1000 km), there are significant differences between the different models. Those identified as “low-amplitude” models in this depth range (S40RTS, S20RTS, SAW642ANb, and S362ANI) resolve the cratons, particularly in the northern hemisphere. However, little short wavelength structure either within the cratons or along their boundaries is resolved. The “higher amplitude” class of models captures stronger heterogeneity, both within and along the craton boundaries.

SL2013sv captures the greatest detail of these strong structural boundaries: the cratons in South America (which are also clear in the tectonic regionalization), the cratonic blocks in southern Africa, the clear signature of the Indian lithosphere underthrusting beneath the Himalaya and western Tibet, and the very narrow high-velocity subducting oceanic lithosphere along the trenches around much of the western Pacific. In addition, we highlight finer scale structural heterogeneity resolved along the western boundary of the North American craton, which improves upon past continental-scale models (Frederiksen et al. 2001; van der Lee and Frederiksen 2005; Nettles and Dziewónski 2008; Bedle and van der Lee 2009) and correlates well with the results of regional-scale high-resolution imaging studies using the USArray (e.g. Sigloch 2011; Tian et al. 2011; Shen et al. 2013; Obrebski et al. 2011; Burdick et al. 2012).

At depths near the base of the continental lithospheric mantle, the strength of heterogeneity is beginning to decrease, as is indicated by the RMS of the shear-wave velocity distribution (Fig. 1.12). At 250 km depth in SL2013sv, LH2008, S40RTS, S20RTS, S362ANI, and DR2012, most anomalies associated with the deep cratonic lithospheric roots have disappeared; what remains is only slightly elevated velocities beneath the continents and larger slightly negative velocity anomalies beneath the oceans. Alternatively, SEMum, CUB, and SAW642ANb show strong fast anomalies persisting to greater depths beneath most continents. These disappear by 350 km in SAW642ANb and, mostly, in SEMum (although an anomaly remains beneath the western African craton). In this depth range, subducting oceanic lithosphere is seen clearly, particularly around the margin of the western Pacific. Broad high-velocity anomalies can be seen in this region in all the models, although they are more focused in SL2013sv and LH2008. In SL2013sv, the highest velocity anomalies correlate well with the superimposed plate boundaries, especially along the Izu-Bonin and Marianas, and south along Sumatra.

The low velocities associated with the East African Rift (and nearby Afar and Red Sea) are consistent between most of the different models. At depths down to 150 km, SL2013sv, LH2008, DR2012, CUB, and SEMum all display a relatively strong, linear negative anomaly underlying the Red Sea; S40RTS, S362ANI, SAW642ANb, and S20RTS also show a negative anomaly, although it is somewhat more circular to oblate. At greater depths down 250–350 km, the low-velocity anomaly stretches from afar southwards along the East African Rift. It is most clear in SL2013sv and SEMum, although still present in the other models, with much lower amplitude.

In the transition zone, the length-scale of heterogeneity imaged increases. At 500 km depth (Fig. 1.19), high-velocity anomalies are imaged in the western Pacific, related to the subduction of the Pacific oceanic lithosphere. There are large differences in the amplitude of the anomalies observed in each of the models and the location of slab anomalies, even at the longer wavelengths (i.e.  $\geq 3000$  km). The inclusion of many *S* and multiple *S* body waves in SL2013sv has enabled improved resolution of high-velocity slabs in the upper mantle, from lithospheric depths through to the transition zone (Schaeffer and Lebedev 2013). We can see the effect of this increase by comparing LH2008 and SL2013sv, which are

generated using the same methodology; however, SL2013sv uses an order of magnitude more seismograms and applies less smoothing at transition zone depths.

## 1.7 Conclusions

Variations in seismic wave velocities provide insight into heterogeneity in the composition and physical state of the rocks within the Earth. The seismic-velocity heterogeneity can be observed in a number of different ways, each offering a complementary perspective on the bulk properties, structure, and dynamics of the Earth.

Our large new data set of global measurements of phase and group velocities permits construction of the dispersion diagram of surface waves on the Earth, spanning a broad period range from  $\sim 10$  to  $> 400$  s. In the Rayleigh-wave diagram presented in this paper, 12 higher modes (overtones) are clearly mapped, in addition to the fundamental mode. The greatest variability is observed at shorter periods for the fundamental mode ( $T < 30$  s for phase velocities;  $T < 40$  s for group velocities), reflecting the higher heterogeneity in the crust–uppermost mantle depth range compared to that in deeper upper mantle.

Global tomographic models constrained with data sets including surface waves have shown agreement at long wavelengths (thousands of kilometres) since 1990s (e.g. Becker and Boschi 2002). Today, a number of recent models show close agreement in the upper 200 km of the mantle at much shorter scale lengths (several hundreds of kilometres). The agreement includes the large amplitudes of shear-speed variations (over  $\pm 10\%$ ) in the lithosphere–asthenosphere depth range. In the deep upper mantle and transition zone, greater disagreements between different available models still remain.

The model SL2013sv (Schaeffer and Lebedev 2013), constrained by an unprecedentedly large data set of multimode waveform fits, displays increased resolution compared to other existing models for many upper-mantle and crustal features across the globe. For many cratons, the boundaries of their high-velocity lithospheres at mantle depths are seen closely following their boundaries at the surface. Important exceptions include low velocities beneath cratons whose lithosphere was modified (e.g. NE China, Wyoming) and very high velocities in cratonic mantle–lithosphere recently underthrust beneath thick orogenic crust (Tibet, Zagros) (e.g. Agius and Lebedev, manuscript in revision, 2013). The model also resolves in detail the structure of the mid-ocean ridges, with the partial-melting induced low-velocity anomalies being very narrow in the uppermost mantle beneath the ridge axis and broadening with depth down to 100–120 km. Sharp shear-speed contrasts at crustal and mantle–lithosphere depths closely match tectonic boundaries at the surface in regions undergoing active deformation, such as Tibet and surroundings or western North America. The model thus captures regional-scale heterogeneity globally, within both the upper mantle and the crust.

Regionalization of SL2013sv by means of clustering (Lekić and Romanowicz 2011b) offers another perspective on upper-mantle heterogeneity. Sorting all locations around the globe into six clusters according to the shear-wave speed profiles at 30–350 km depths beneath them, with no *a priori* information, we obtain an accurate tectonic regionalization of the entire Earth. Oceanic locations fall into three clusters distinguished by the lithospheres maturity: youngest oceans, ridges and backarcs (hot or wet mantle with partial melt likely at many places; very low  $V_S$ ), ancient oceanic basins (cold, high-velocity lithospheres), and intermediate-aged oceans, including portions of old oceanic lithosphere that were “rejuvenated” when passing over hot spots. The continents also split into three clusters: cratons (cold, deep, high-velocity lithospheric roots), intermediate continents, including Precambrian fold belts or cratons modified in the Proterozoic, and Phanerozoic continents (the latter containing almost all recent continental volcanism).

A global stack of 1D shear-speed profiles through the crust and upper mantle shows a monotonic decrease in the amplitude of wave speed variations with depth. This is mirrored by a decrease in RMS variations—from large in the top 150–200 km to much smaller below 250 km—seen in all the tomographic models compared.

The “depth of tectonics”—depths down to which differences between shear-wave speed profiles under oceanic and continental lithospheres of different ages persist (Jordan and Paulson 2013)—can be estimated from the type-average profiles given by the cluster analysis of the global shear-wave speed heterogeneity (Fig. 1.8). Young oceans display the lowest velocities among oceanic regions in the uppermost mantle. The intermediate-age-ocean average profile does not differ substantially from the young ocean one at depths of 150 km and greater but is similar to the old ocean profile in the upper 50 km of the mantle. The oldest oceans show higher shear-wave speeds than young and intermediate ones down to ~200 km depth. Phanerozoic and intermediate-age continents’ profiles converge with each other and with the oceanic profiles at 200–250 km depth. The oldest continents (cratons) stand out to the greatest depth, with shear-wave speeds beneath them higher than beneath all other regions, on average, down to 250–280 km depths.

**Acknowledgments** Insightful comments by Li Zhao and Frédéric Deschamps have helped us to improve the manuscript. We thank the creators of the tomographic models compared in this study for making them available. Waveform data used for the construction of the model SL2013sv were obtained from the facilities of IRIS, ORFEUS, GFZ, and CNSN. We are grateful to the operators of the many networks used in this study. All figures were generated using Generic Mapping Tools (GMT; Wessel and Smith 1995). This work was supported by Science Foundation Ireland (Grant 09/RFP/GEO2550), with additional support by Science Foundation Ireland and the Marie-Curie Action COFUND (Grant Number 11/SIRG/E2174). Our tomographic model, SL2013sv, can be downloaded from <http://www.dias.ie/~aschaeff/SL2013sv.html>.

## References

- Adam JM-C, Lebedev S (2012) Azimuthal anisotropy beneath southern Africa from very broad-band surface-wave dispersion measurements. *Geophys J Int* 191(1):155–174
- Aki K, Christoffersen A, Husebye ES (1977) Determination of the three-dimensional seismic structure of the lithosphere. *J Geophys Res* 82:(277–296)
- Amaru ML (2006) Global travel time tomography with 3-D reference models. PhD thesis, Universiteit Utrecht
- Babuska V, Cara M (1991) Seismic anisotropy in the earth. Kluwer Academic Press, Boston
- Bassin C, Laske G, Masters G (2000) The current limits of resolution for surface wave tomography in North America. *EOS* 81:F897
- Becker TW, Boschi L (2002) A comparison of tomographic and geodynamic mantle models. *Geochem Geophys Geosys* 3
- Bedle H, van der Lee S (2009) S velocity variations beneath North America. *J Geophys Res* 114(B7)
- Bijwaard H, Spakman W, Engdahl ER (1998) Closing the gap between regional and global travel time tomography. *J Geophys Res* 103(B12):30055–30078
- Boschi L, Ekström G (2002) New images of the Earths upper mantle from measurements of surface wave phase velocity anomalies. *J Geophys Res* 107(B4)
- Bozdag E, Trampert J (2008) On crustal corrections in surface wave tomography. *Geophys J Int* 172:1066–1082
- Burdick S, van der Hilst RD, Vernon FL, Martynov V, Cox T, Eakins J, Karasu G, Tylell J, Astiz L, Pavlis GL (2012) Model update March 2011: upper mantle heterogeneity beneath North America from traveltimes tomography with global and USAArray Transportable Array data. *Seismol Res Lett* 83(1):23–28
- Chevrot S, Zhao L (2007) Multiscale finite-frequency Rayleigh wave tomography of the Kaapvaal craton. *Geophys J Int* 169:201–215
- Dahlen FA, Tromp J (1998) Theoretical global seismology. Princeton University Press, Princeton
- Darbyshire FA, Lebedev S (2009) Rayleigh wave phase-velocity heterogeneity and multilayered azimuthal anisotropy of the Superior Craton, Ontario. *Geophys J Int* 176:215–234
- Debayle E, Ricard Y (2012) A global shear velocity model of the upper mantle from fundamental and higher Rayleigh mode measurements. *J Geophys Res* 117(B10):1–24
- Debayle E, Kennett BLN, Priestley K (2005) Global azimuthal seismic anisotropy and the unique plate-motion deformation of Australia. *Nature* 433(7025):509–512
- Deschamps F, Lebedev S, Meier T, Trampert J (2008) Stratified seismic anisotropy reveals past and present deformation beneath the East-central United States. *Earth Planet Sci Lett* 274(3–4):489–498
- Dziewonski AM, Anderson DL (1981) Preliminary reference Earth model. *Phys Earth Planet* 25:297–356
- Dziewónski AM, Hager B, O'Connell RJ (1977) Large-scale heterogeneities in the lower mantle. *J Geophys Res* 82:239–255
- Ekström G (2011) A global model of Love and Rayleigh surface wave dispersion and anisotropy, 25–250 s. *Geophys J Int* 187:1668–1686
- Endrun B, Lebedev S, Meier T, Tirel C, Friederich W (2011) Complex layered deformation within the Aegean crust and mantle revealed by seismic anisotropy. *Nat Geosci* 4(3):203–207
- Engdahl ER, van der Hilst RD, Buland R (1998) Global teleseismic earthquake relocation with improved travel times and procedures for depth determination. *B Seismo Soc Am* 88(3):722–743
- Ferreira AMG, Woodhouse JH, Visser K, Trampert J (2010) On the robustness of global radially anisotropic surface wave tomography. *J Geophys Res* 115(B4):1–16
- Forsyth DW, Scheirer D, Webb S, The MELT Seismic Team (1998) Imaging the deep seismic structure beneath a mid-ocean ridge: the MELT experiment. *Science* 280(5367):1215–8

- Frederiksen AW, Bostock MG, Cassidy JF (2001) S-wave velocity structure of the Canadian upper mantle. *Phys Earth Planet* 124:175–191
- Grand SP (2002) Mantle shear-wave tomography and the fate of subducted slabs. *Philos T R Soc Lond* 360:2475–2491
- Gu YJ, Dziewoński AM, Su W, Ekström G (2001) Models of the mantle shear velocity and discontinuities in the pattern of lateral heterogeneities. *J Geophys Res* 106(B6):11169–11199
- Gu YJ, Dziewoński AM, Ekström G (2003) Simultaneous inversion for mantle shear velocity and topography of transition zone discontinuities. *Geophys J Int* 154:559–583
- Gudmundsson O, Cambridge M (1998) A regionalized upper mantle (RUM) seismic model. *J Geophys Res* 103:7121–7136
- Hafkenscheid E, Wortel MJR, Spakman W (2006) Subduction history of the Tethyan region derived from seismic tomography and tectonic reconstructions. *J Geophys Res* 111(B8):1–26
- Houser C, Masters G, Shearer PM, Laske G (2008) Shear and compressional velocity models of the mantle from cluster analysis of long-period waveforms. *Geophys J Int* 174:195–212
- Jordan TH (1981) Global tectonic regionalization for seismological data analysis. *B Seismo Soc Am* 71(4):1131–1141
- Jordan TH, Paulson EM (2013) Convergence depths of tectonic regions from an ensemble of global tomographic models. *J Geophys Res* 118 (B8):4196–4225
- Karason H, van der Hilst RD (2001) Improving global tomography models of P-wavespeed I: incorporation of differential times for refracted and diffracted core phases (PKP, Pdiff). *J Geophys Res* 106:6569–6587
- Kennett BLN (1987) Observational and theoretical constraints on crustal and upper-mantle heterogeneity. *Phys Earth Planet* 47:319–332
- Kennett BLN, Engdahl ER, Buland R (1995) Constraints on seismic velocities in the Earth from traveltimes. *Geophys J Int* 122(1):108–124
- Kovach RL (1979) Seismic surface waves and crustal and upper mantle structure. *Rev Geophys* 1(16):1–13
- Kustowski B, Dziewoński AM, Ekström G (2007) Nonlinear crustal corrections for normal-mode seismograms. *B Seismo Soc Am* 97(5):1756–1762
- Kustowski B, Ekström G, Dziewoński AM (2008) Anisotropic shear-wave velocity structure of the Earth's mantle: a global model. *J Geophys Res* 113(B6):1–23
- Lebedev S, van der Hilst RD (2008) Global upper-mantle tomography with the automated multimode inversion of surface and S-wave forms. *Geophys J Int* 173:505–518
- Lebedev S, Nolet G, Meier T, van der Hilst RD (2005) Automated multimode inversion of surface and S waveforms. *Geophys J Int* 162:951–964
- Lebedev S, Adam J, Meier T (2013) Mapping the Moho with seismic surface waves: a review, resolution analysis, and recommended inversion strategies. *Tectonophysics* (Moho special edition)
- Legendre CP, Meier T, Lebedev S, Friederich W, Viereck-Götte L (2012) A shear wave velocity model of the European upper mantle from automated inversion of seismic shear and surface waveforms. *Geophys J Int* 191:282–304
- Lekić V, Romanowicz B (2011a) Inferring upper-mantle structure by full waveform tomography with the spectral element method. *Geophys J Int* 185(2):799–831
- Lekić V, Romanowicz B (2011b) Tectonic regionalization without a priori information: a cluster analysis of upper mantle tomography. *Earth Planet Sci Lett* 308(1–2):151–160
- Lekić V, Panning M, Romanowicz B (2010) A simple method for improving crustal corrections in waveform tomography. *Geophys J Int* 182:265–278
- Li X-D, Romanowicz B (1996) Global mantle shear velocity model developed using nonlinear asymptotic coupling theory. *J Geophys Res* 101(B10):22245–22272
- Li C, van der Hilst RD, Engdahl ER, Burdick S (2008) A new global model for P wave speed variations in Earth's mantle. *Geochem Geophys Geosys* 9(5):Q05018
- Marone F, Romanowicz B (2007) Non-linear crustal corrections in high-resolution regional waveform seismic tomography. *Geophys J Int* 170(1):460–467

- Masters G, Johnson S, Laske G, Bolton H (1996) A shear-velocity model of the mantle. *Philos T R Soc Lond* 354(1711):1385–1411
- Masters G, Laske G, Bolton H, Dziewónski AM (2000) The relative behavior of shear velocity, bulk sound speed, and compressional velocity in the mantle: implications for chemical and thermal structure, Earth's deep interior: mineral physics and tomography from the atomic to the global scale, pp 63–87
- Mégnin C, Romanowicz B (2000) The three-dimensional shear velocity structure of the mantle from the inversion of body, surface and higher-mode waveforms. *Geophys J Int* 143(3):709–728
- Montagner J-P, Tanimoto T (1991) Global upper mantle tomography of seismic velocities and anisotropies. *J Geophys Res* 96(B12):20337–20351
- Montelli R, Nolet G, Masters G, Dahlen FA, Hung S-H (2004) Global P and PP traveltimes tomography: rays versus waves. *Geophys J Int* 158(2):637–654
- Mooney WD, Laske G, Masters G (1998) Crust 5.1: a global crustal model at  $5^\circ \times 5^\circ$ . *J Geophys Res* 103(B1):727–747
- Muller RD, Roest WR, Royer J-Y, Gahagan LM, Sclater JG (1997) Digital isochrons of the world's ocean floor. *J Geophys Res* 102(B2):3211–3214
- Nataf H, Ricard Y (1996) 3SMAC: an a priori tomographic model of the upper mantle based on geophysical modeling. *Phys Earth Planet* 92(1):95
- Nettles M, Dziewónski AM (2008) Radially anisotropic shear velocity structure of the upper mantle globally and beneath North America. *J Geophys Res* 113(B2):1–27
- Nolet G (1990) Partitioned waveform inversion and two-dimensional structure under the network of autonomously recording seismographs. *J Geophys Res* 95(B6):8499–8512
- Nolet G (2008) A breviary of seismic tomography. Cambridge University Press, Cambridge
- Nolet G, Grand SP, Kennett BLN (1994) Seismic heterogeneity in the upper mantle. *J Geophys Res* 99(B12):23753–23766
- Obrebski M, Allen RM, Pollitz F, Hung S-H (2011) Lithosphere-asthenosphere interaction beneath the western United States from the joint inversion of body-wave traveltimes and surface-wave phase velocities. *Geophys J Int* 185(2):1003–1021
- Panning MP, Romanowicz B (2006) A three-dimensional radially anisotropic model of shear velocity in the whole mantle. *Geophys J Int* 167(1):361–379
- Panning MP, Lekić V, Romanowicz Ba (2010) Importance of crustal corrections in the development of a new global model of radial anisotropy. *J Geophys Res* 115(B12):B12325
- Ritsema J, van Heijst HJ, Woodhouse JH (1999) Complex shear wave velocity structure imaged beneath Africa and Iceland. *Science* 286:1925–1928
- Ritsema J, van Heijst HJ, Woodhouse JH (2004) Global transition zone tomography. *J Geophys Res* 109(B2)
- Ritsema J, Deuss A, van Heijst HJ, Woodhouse JH (2011) S40RTS: a degree-40 shear-velocity model for the mantle from new Rayleigh wave dispersion, teleseismic traveltimes and normal-mode splitting function measurements. *Geophys J Int* 184(3):1223–1236
- Schaeffer AJ, Lebedev S (2013) Global shear speed structure of the upper mantle and transition zone. *Geophys J Int* 194(1):417–449
- Shapiro NM, Ritzwoller MH (2002) Monte-Carlo inversion for a global shear-velocity model of the crust and upper mantle. *Geophys J Int* 151(1):88–105
- Shen W, Ritzwoller MH, Schulte-Pelkum V (2013) A 3-D model of the crust and uppermost mantle beneath the central and western US by joint inversion of receiver functions and surface wave dispersion. *J Geophys Res* 118:1–15
- Siebert L, Simkin T (2002) Volcanoes of the World: an Illustrated catalog of holocene volcanoes and their eruptions
- Sigloch K (2011) Mantle provinces under North America from multifrequency P wave tomography. *Geochem Geophys Geosys* 12(2):1–27
- Simmons NA, Myers SC, Johannesson G, Matzel E (2012) LLNL-G3Dv3: Global P wave tomography model for improved regional and teleseismic travel time prediction. *J Geophys Res* 117(B10):1–28

- Steinberger B (2000) Plumes in a convecting mantle: models and observations for individual hot-spots. *J Geophys Res* 105(B5):11127–11152
- Su W-J, Woodward R, Dziewoński AM (1992) Deep origin of mid-ocean-ridge seismic velocity anomalies. *Nature* 360:149–152
- Su W-J, Woodward R, Dziewoński AM (1994) Degree 12 model of shear velocity heterogeneity in the mantle. *J Geophys Res* 99(B4):6945–6980
- Tian Y, Zhou Y, Sigloch K, Nolet G, Laske G (2011) Structure of North American mantle constrained by simultaneous inversion of multiple-frequency SH, SS, and Love waves. *J Geophys Res* 116(B2):1–18
- van der Lee S, Frederiksen AW (2005) Surface wave tomography applied to the North American upper mantle. In: Levander A, Nolet G (eds) *Seismic earth: array analysis of broadband seismograms*, vol 157, pp 67–80. AGU Geophysical Monograph Series, Washington, DC
- Wang Z, Dahlen FA (1995) Spherical-spline parameterization of three-dimensional Earth models. *Geophys Res Lett* 22(22):3099–3102
- Wessel P, Smith W (1995) New version of the generic mapping tools released. *EOS* 76:329
- Woodhouse JH, Dziewoński AM (1984) Mapping the upper mantle: three-dimensional modeling of earth structure by inversion of seismic waveforms. *J Geophys Res* 89(B7):5953–5986
- Wu RS, Flatté SM (1990) Transmission fluctuations across an array and heterogeneities in the crust and upper mantle. *Pure Appl Geophys* 132:175–196
- Zhang Y, Tanimoto T (1992) Ridges, hotspots and their interaction as observed in seismic velocity maps. *Nature* 355:45–49
- Zhang Y, Tanimoto T (1993) High-resolution global upper mantle structure and plate tectonics. *J Geophys Res* 98(B6):9793–9823
- Zhang X, Paulssen H, Lebedev S, Meier T (2009) 3D shear velocity structure beneath the Gulf of California from Rayleigh wave dispersion. *Earth Planet Sci Lett* 279(3–4):255–262
- Zhou Y, Nolet G, Dahlen Fa, Laske G (2006) Global upper-mantle structure from finite-frequency surface-wave tomography. *J Geophys Res* 111(B4):1–24